Moment gas kinetic flux solver for simulation of flows from continuum regime to rarefied regime

Zhenyu Yuan (袁震宇)[1] and Chang Shu (舒昌)[2,*]
[1]*School of Energy and Power Engineering, Nanjing University of Science and Technology, Nanjing 210094, China*
[2]*Department of Mechanical Engineering, National University of Singapore, 10 Kent Ridge Crescent 119260, Singapore*

(Received 30 August 2025; accepted 17 April 2026; published 22 June 2026)

This paper proposes the moment gas kinetic flux solver (MGKFS) for the simulation of flows from a continuum regime to a rarefied regime. Its fundamental innovation lies in the dual-flux strategy, which extends the conventional gas kinetic flux solver (GKFS) paradigm by directly calculating numerical fluxes not only for the conservation equations (mass, momentum, and energy) but also for the high-order moment equations (stress and heat flux) at cell interfaces. Thus, MGKFS effectively overcomes the critical limitation identified in the Grad-13-based GKFS (G13-GKFS). G13-GKFS locally interpolates stress and heat flux at cell centers from their values at cell interfaces. This approach neglects their global evolution equations, leading to insufficient global accuracy. MGKFS directly captures the evolution of these high-order moments with flux reconstruction from the local solution of the Boltzmann equation at the cell interface. Numerical validations demonstrate that MGKFS significantly outperforms G13-GKFS, achieving superior accuracy. This improvement is particularly notable in boundary layers, where global fidelity is essential.

DOI: 10.1103/2grk-9fqf

I. INTRODUCTION

Rarefied gas dynamics holds significant importance in aerospace engineering [1,2], micro-electromechanical systems [3,4], and vacuum technology applications [5,6]. Consequently, the numerical method has progressively evolved, transitioning from addressing Navier-Stokes equations to tackling the Boltzmann equation. The numerical approaches for rarefied flows can be clarified into stochastic and deterministic methods. The direct simulation Monte Carlo [7,8] (DSMC), Fokker-Planck method [9,10], and wave-particle method [11–13] all belong to stochastic methods. These methods are highly accurate for simulating rarefied flows. However, they necessitate multistep averaging processes to reduce the statistical noise arising from random uncertainty.

In contrast to stochastic approaches, deterministic methods, such as the discrete velocity method [14,15] (DVM) and Grad's series moment methods [16–18], achieve results without requiring statistical averaging for noise reduction. The representative DVMs are the unified gas kinetic scheme [19,20] (UGKS), the general synthetic iterative scheme [21,22] (GSIS), the discrete unified gas kinetic scheme [23,24] (DUGKS), and so on. When comparing computational efficiency, the Grad's moment method demonstrates superior performance to DVM. This efficiency advantage stems from their fundamental differences in governing equations: DVM resolves mesoscopic equations, requiring discretization in both velocity space and physical space, whereas the Grad's moment

*Contact author: mpeshuc@nus.edu.sg

method operates through macroscopic equations (conservation laws coupled with high-order moment equations), thereby eliminating velocity space dependencies. Regarding implementation complexity, DVM exhibits significantly simpler computational realization compared to the Grad's moment method. The complexity of the Grad's moment method mainly arises from its requirement to handle intricate systems of partial differential equations (PDEs). Developing robust numerical schemes for these high-order PDEs presents substantial challenges. Furthermore, these complex PDE systems necessitate complicated boundary conditions, substantially increasing implementation difficulties when applying Grad's moment methods to geometrically complex configurations.

To combine the advantages of DVM and the moment method, the Grad function-based gas kinetic flux solver [25,26] (Grad-GKFS) and Grad function-based gas kinetic scheme (Grad-GKS) [27] were proposed. For simplicity, these approaches typically adopt the Grad 13 distribution function; we therefore refer to them as the flux solver variant G13-GKFS. In one aspect, G13-GKFS reconstructs the local solution of the Boltzmann equation at each cell interface and employs the Grad 13 distribution function (derived via third-order Hermite polynomial expansion) as the initial guess of the distribution function at surrounding points of the cell interface, thus avoiding the discretization in velocity space. In another aspect, the high-order moments (such as stress tensor and heat flux) involved in the Grad 13 distribution function are calculated through moment relationships, thus avoiding solving the tedious high-order PDEs for high-order moments. Current applications by Liu *et al*. [28] demonstrate the potential of G13-GKFS in microscale flows. Benchmark simulations of lid-driven cavity flow at the Knudsen number of 0.0798 reveal excellent agreement of velocity profiles with DVM data. However, comparative analysis shows persistent discrepancies in temperature, stress tensor, and heat flux predictions between G13-GKFS and DVM results, suggesting that the G13-GKFS requires further theoretical refinement. Additionally, the poor performance of G13-GKFS mainly occurs inside the boundary layer or in the corner region. Taking the results from Ref. [29] as an example, G13-GKFS underestimates the temperature near the position of the left upper corner and overestimates the temperature near the position of the right upper corner for the lid-driven cavity flow.

Furthermore, the observed discrepancies in G13-GKFS performance manifest in high-order moments, prompting the need to investigate the underlying causes of these computational inaccuracies. To systematically address this issue, it is imperative to concentrate on analyzing the numerical algorithms and implementation details specifically for high-order moments within the G13-GKFS framework. As mentioned above, G13-GKFS employs moment relationships to determine the high-order moments at cell interfaces, subsequently deriving cell-centered values through interpolation techniques. Thus, the current method demonstrates localized accuracy in resolving high-order moment solutions, but it critically fails to ensure global fidelity[1] throughout the computational domain. In other words, the current G13-GKFS effectively circumvents the direct solution of high-order partial differential equations (PDEs) in 13-moment equations, but it ignores the evolution process of high-order moments. This inherent limitation raises a pivotal question: Can we develop a numerical scheme that directly addresses the evolutionary dynamics of high-order moments involved in 13-moment equations?

The solution to this problem lies in reexamining a key feature of conventional GKFS: its innovative flux construction mechanism based on the distribution function at the interface. Conventional GKFS essentially solves the five macroscopic conservation equations (mass, momentum, and energy) by using the finite volume method (FVM). Their numerical fluxes at the cell interface are evaluated by the moments of the distribution function. This strategy can be extended to solve the evolution equations for stress tensors and heat fluxes.

[1]"global fidelity" refers to the property that the solution for a variable (especially high-order moments like stress tensor and heat flux) satisfies its own evolution equation throughout the entire computational domain, not just locally at interfaces.

In this paper, we propose a moment gas kinetic flux (MGKFS) solver. Like conventional GKFS, the governing equations for conservative variables (mass, momentum, and energy) are still solved by the FVM. In addition, a set of evolution equations for stresses and heat fluxes is also solved by the FVM, in which numerical fluxes of stress and heat flux are evaluated by high-order moments of the distribution function at cell interfaces. In other words, the high-order moment equations are not approximated by macroscopic constitutive relations or derivatives. Instead, they are directly computed via moment integration of a reconstructed gas distribution function at cell interfaces. Thus, this strategy not only provides a new closure method for the 13-moment system but also avoids the treatment of tedious boundary conditions for stress and heat flux equations. The proposed method is validated using benchmark cases, including lid-driven cavity flow, bottom-heated cavity flow, and temperature gradient-driven flow. Numerical validations demonstrate that the solver achieves robust performance for flows from the continuum regime to the rarefied regime. Comparative analyses reveal the superior accuracy of the present method over G13-GKFS in predicting critical parameters such as temperature, stress tensor, and heat flux. These improvements are particularly notable in boundary layer regions.

The remainder of this work is structured as follows. Section II establishes the theoretical foundation by showing the intrinsic relationship between the Boltzmann equation and macroscopic governing equations. Section III provides an overview of the conventional GKFS and G13-GKFS. The proposed methodology is systematically detailed in Sec. IV, including four critical components: (1) formulation of microscopic equations for moment systems, (2) derivation of numerical fluxes for stress tensor and heat flux, (3) implementation of boundary conditions, and (4) comprehensive computational procedure. Section V presents numerical validations across multiscale flow scenarios, followed by comparative analyses with existing methods. Finally, Sec. VI concludes.

II. GAS KINETIC THEORY

A. Boltzmann equation

The Boltzmann equation describes the evolution of the gas distribution function under the influence of streaming and collisions from the mesoscopic level. For simplicity, its collision term can be approximated by the Bhatnagar–Gross–Krook (BGK) collision model, and the Boltzmann equation can be written as

$$\frac{\partial f}{\partial t} + \vec{\xi} \cdot \frac{\partial f}{\partial \vec{x}} = \frac{g - f}{\tau}, \tag{1}$$

where f is the distribution function of gas particles, which is the function of position $\vec{x} = (x, y, z)$, particle velocity $\vec{\xi} = (\xi_x, \xi_y, \xi_z)$, and time t. τ means the relaxation time, which is the ratio of macroscopic gas viscosity μ and pressure p. g is the equilibrium distribution function, and is often taken as a Maxwell distribution as follows:

$$g = \frac{\rho}{(2\pi RT)^{3/2}} \exp\left(-\frac{{C_x}^2 + {C_y}^2 + {C_z}^2}{2RT}\right). \tag{2}$$

Here, ρ is the macroscopic density, T is the macroscopic temperature, and R is the gas constant. C_x, C_y, and C_z are the peculiar velocity in the x-, y-, and z-directions, respectively. Their values can be calculated by the difference between the particle velocities and macroscopic velocities as follows:

$$C_x = \xi_x - U, \quad C_y = \xi_y - V, \quad C_z = \xi_z - W, \tag{3}$$

in which, U, V, and W represent the macroscopic velocity in the x-, y-, and z- directions, respectively.

B. Macroscopic governing equations

The moment relationships are bridges that connect the Boltzmann equation and macroscopic governing equations. By multiplying f and g with the moment vector

$$\overrightarrow{\varphi} = \left[1, \quad \xi_x, \quad \xi_y, \quad \xi_z, \quad \tfrac{1}{2}|\vec{\xi}|^2\right]^T, \tag{4}$$

and integrating them in the particle velocity space, we can obtain the relations as follows:

$$\begin{bmatrix} \rho \\ \rho U \\ \rho V \\ \rho W \\ \rho E \end{bmatrix} = \begin{bmatrix} \langle f \rangle \\ \langle f \cdot \xi_x \rangle \\ \langle f \cdot \xi_y \rangle \\ \langle f \cdot \xi_z \rangle \\ \frac{1}{2}\langle f \cdot |\vec{\xi}|^2 \rangle \end{bmatrix} = \begin{bmatrix} \langle g \rangle \\ \langle g \cdot \xi_x \rangle \\ \langle g \cdot \xi_y \rangle \\ \langle g \cdot \xi_z \rangle \\ \frac{1}{2}\langle g \cdot |\vec{\xi}|^2 \rangle \end{bmatrix}. \tag{5}$$

Here, E is the total energy and related to the velocity and temperature as follows:

$$E = (U^2 + V^2 + W^2)/2 + RT/(\gamma - 1), \tag{6}$$

where γ is the specific heat ratio and is equal to $5/3$ for a monatomic gas.

It is noteworthy that the operator $\langle \ldots \rangle$ represents the integration over the whole velocity space as follows:

$$\langle \ldots \rangle = \int_{-\infty}^{+\infty} \int_{-\infty}^{+\infty} \int_{-\infty}^{+\infty} (\ldots) d\xi_x d\xi_y d\xi_z. \tag{7}$$

Similarly, by multiplying Eq. (1) with the moment vector shown in Eq. (4) and then integrating the resultant equation in the whole velocity space, the macroscopic governing equations can be derived,

$$\frac{\partial \vec{W}}{\partial t} + \frac{\partial \vec{F}_x}{\partial x} + \frac{\partial \vec{F}_y}{\partial y} + \frac{\partial \vec{F}_z}{\partial z} = 0, \tag{8}$$

where $\vec{W} = (\rho, \rho U, \rho V, \rho W, \rho E)^T$ is the vector of macroscopic conservative variables. Their values are computed by the relevant moments of distribution function f as shown in Eq. (5). $\vec{F}_x$, $\vec{F}_y$, and $\vec{F}_z$ are calculated by

$$\vec{F}_x = \langle \xi_x \cdot \overrightarrow{\varphi} \cdot f \rangle, \quad \vec{F}_y = \langle \xi_y \cdot \overrightarrow{\varphi} \cdot f \rangle, \quad \vec{F}_z = \langle \xi_z \cdot \overrightarrow{\varphi} \cdot f \rangle. \tag{9}$$

By substituting the expression of $\overrightarrow{\varphi}$ into $\vec{F}_x$, we can obtain the expressions as follows (The details for this process can be seen in Appendix):

$$\vec{F}_x = \begin{bmatrix} F_x^{\rho} \\ F_x^{\rho U} \\ F_x^{\rho V} \\ F_x^{\rho W} \\ F_x^{\rho E} \end{bmatrix} = \begin{bmatrix} \langle \xi_x \cdot f \rangle \\ \langle \xi_x \cdot \xi_x \cdot f \rangle \\ \langle \xi_x \cdot \xi_y \cdot f \rangle \\ \langle \xi_x \cdot \xi_z \cdot f \rangle \\ \frac{1}{2}\langle \xi_x \cdot |\vec{\xi}|^2 \cdot f \rangle \end{bmatrix} = \begin{bmatrix} \rho U \\ \rho U^2 + p + \sigma_{xx} \\ \rho UV + \sigma_{xy} \\ \rho UW + \sigma_{xz} \\ U(\rho E + p) + \sigma_{xx} U + \sigma_{xy} V + \sigma_{xz} W + q_x \end{bmatrix}. \tag{10}$$

Then, the expressions for $\vec{F}_y$ and $\vec{F}_z$ can also be derived (as seen in Appendix). Finally, Eq. (8) can be further expressed as

$$\frac{\partial}{\partial t} \begin{bmatrix} \rho \\ \rho \mathbf{u} \\ \rho E \end{bmatrix} + \nabla \cdot \begin{bmatrix} \rho \mathbf{u} \\ \rho \mathbf{u}\mathbf{u} + p\mathbf{I} \\ (\rho E + p)\mathbf{u} \end{bmatrix} + \nabla \cdot \begin{bmatrix} 0 \\ \mathbf{\Pi} \\ \mathbf{\Pi} \cdot \mathbf{u} + \mathbf{Q} \end{bmatrix} = 0. \tag{11}$$

Equation (11) is the conservative equations for mass, momentum, and energy. Its expressions are the same as the well-known Navier-Stokes equations, in which $\mathbf{u}$, $\mathbf{\Pi}$, and $\mathbf{Q}$ represent the

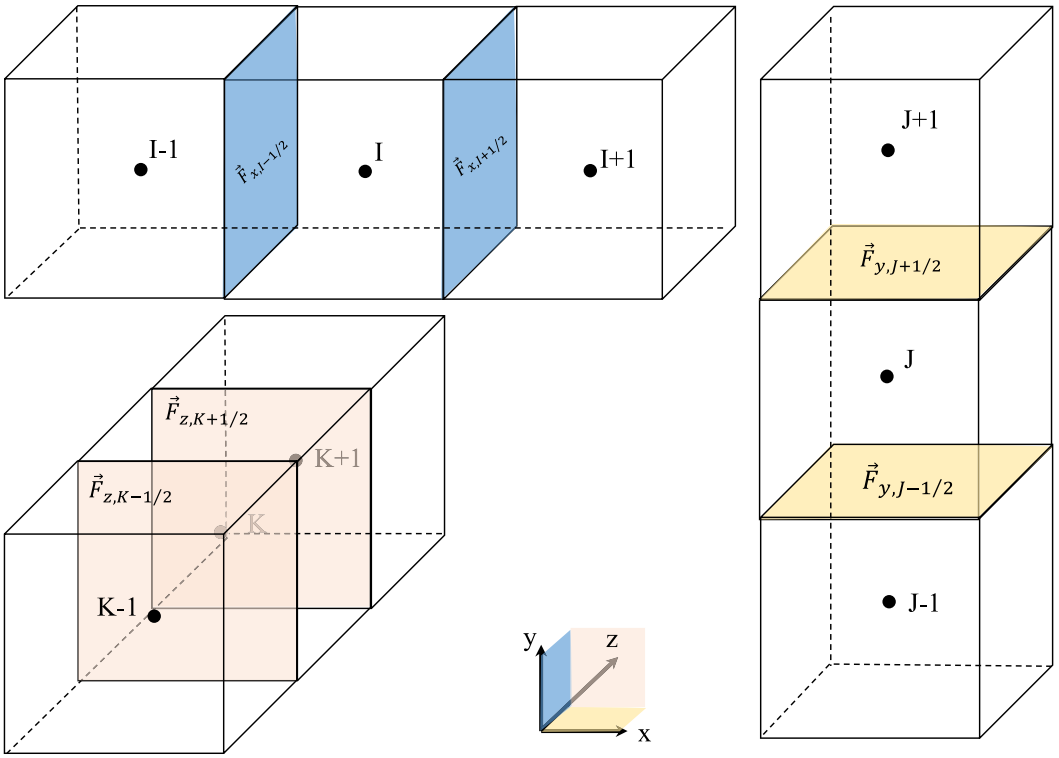

FIG. 1. Schematic of flux vectors at cell interfaces.

velocity vector, stress tensor, and heat flux vector, respectively. Their expansion components can be written as

$$\mathbf{u} = \begin{bmatrix} U \\ V \\ W \end{bmatrix}, \quad \mathbf{\Pi} = \begin{bmatrix} \sigma_{xx} & \sigma_{xy} & \sigma_{xz} \\ \sigma_{yx} & \sigma_{yy} & \sigma_{yz} \\ \sigma_{zx} & \sigma_{zy} & \sigma_{zz} \end{bmatrix}, \quad \mathbf{Q} = \begin{bmatrix} q_x \\ q_y \\ q_z \end{bmatrix}. \tag{12}$$

III. GAS KINETIC FLUX SOLVER

A. Conventional gas kinetic flux solver

The gas kinetic flux solver is established on the framework of the finite volume method (FVM). By integrating Eq. (8) over a control volume $\Delta V = \Delta x \cdot \Delta y \cdot \Delta z$, it can be reformulated as

$$\vec{W}^{n+1} = \vec{W}^{n} - \frac{\Delta t}{\Delta V} \begin{bmatrix} (\vec{F}_{x,I+1/2} - \vec{F}_{x,I-1/2}) \cdot \Delta y \cdot \Delta z \\ +(\vec{F}_{y,J+1/2} - \vec{F}_{y,J-1/2}) \cdot \Delta x \cdot \Delta z \\ +(\vec{F}_{z,K+1/2} - \vec{F}_{z,K-1/2}) \cdot \Delta x \cdot \Delta y \end{bmatrix}, \tag{13}$$

where Δx, Δy, and Δz denote the length of control volume in the x-, y-, and z-directions, respectively. As shown in Fig. 1, $\vec{F}_{x,I-1/2}$ represents the flux vectors on the interface between cell $I-1$ and cell I. $\vec{F}_{x,I+1/2}$ denotes the flux vectors on the interface between cell I and cell $I+1$. These fluxes are computed via moment integration of the gas distribution function $f_{I\pm1/2}$ at the corresponding interface. Thus, for the x-direction interface, the flux is expressed as

$$\vec{F}_{x,I\pm1/2} = \langle \xi_x \cdot \overrightarrow{\varphi} \cdot f_{I\pm1/2} \rangle. \tag{14}$$

The flux calculation for the y-direction ($\vec{F}_{y,J\pm1/2}$) and the z-direction ($\vec{F}_{z,K\pm1/2}$) follows identical principles to the x-direction implementation and is therefore omitted for brevity. The conservative variables are discretized as $\vec{W}^n$ (current time step) and $\vec{W}^{n+1}$ (subsequent time step), representing the evolution process. Thus, Eq. (13) exactly solves Eq. (11).

The critical challenge in computing numerical fluxes at cell interfaces lies in the accurate reconstruction of the distribution function at these interfacial locations. To illustrate this process, we can take the flux vector $\vec{F}_{x,I+1/2}$ as an example. Based on the BGK model presented in Eq. (1), the gas distribution function at the interface can be mathematically derived as [30]

$$f(\boldsymbol{x}_{I+1/2},\boldsymbol{\xi},t+\Delta t)=\frac{\tau}{\tau+\Delta t}f(\boldsymbol{x}_{I+1/2}-\boldsymbol{\xi}\Delta t,\boldsymbol{\xi},t)+\frac{\Delta t}{\tau+\Delta t}g(\boldsymbol{x}_{I+1/2},\boldsymbol{\xi},t+\Delta t), \tag{15}$$

where $f(\boldsymbol{x}_{I+1/2}-\boldsymbol{\xi}\Delta t,\boldsymbol{\xi},t)$ represents the initial distribution function at the surrounding points of the cell interface, which fundamentally governs the predictive capability of the gas kinetic scheme. $g(\boldsymbol{x}_{I+1/2},\boldsymbol{\xi},t+\Delta t)$ is the equilibrium distribution function at the cell interface, which is dependent on local density, velocity, and temperature as shown in Eq. (2). It is noteworthy that the streaming time step Δt in the solution reconstruction at the cell interface should be specified. The main constraint here is to make sure the local constructing points are within the neighboring cells. To satisfy this criterion, it can be determined by $\Delta t \leqslant 0.5\Delta x/\max\{|\boldsymbol{\xi}|\}$ for a uniform mesh and $\max\{|\boldsymbol{\xi}|\}$ is the maximum discrete velocity. Based on the compatibility condition, we can derive that conservative macroscopic variables at the cell interface can be calculated by the initial distribution function as follows:

$$\vec{W}_{I+1/2}=\langle\overrightarrow{\varphi}\cdot f(\boldsymbol{x}_{I+1/2}-\boldsymbol{\xi}\Delta t,\boldsymbol{\xi},t)\rangle. \tag{16}$$

In a conventional gas kinetic flux solver, the initial distribution function $f(\boldsymbol{x}_{I+1/2}-\boldsymbol{\xi}\Delta t,\boldsymbol{\xi},t)$ is typically approximated using the first-order Chapman-Enskog (CE) expansion [31] and expressed as

$$f^{NS}(\boldsymbol{x}_{I+1/2}-\boldsymbol{\xi}\Delta t,\boldsymbol{\xi},t)=g-\tau Dg. \tag{17}$$

Yuan *et al*. [32] further refined this expression to

$$f^{NS}=g\left[1+\frac{C_iC_j}{2pRT}\left(-2\mu\frac{\partial U_{<i}}{\partial x_{j>}}\right)+\frac{C_i}{pRT}\left(\frac{C^2}{5RT}-1\right)\cdot\left(-\lambda\frac{\partial T}{\partial x_i}\right)\right], \tag{18}$$

where p denotes the pressure, and μ and λ are the viscosity and thermal conductivity coefficients, respectively. $\partial U_{<i}/\partial x_{j>}$ and $\partial T/\partial x_i$ are the velocity and temperature gradients. This first-order CE expansion incorporates linearized stress tensor and heat flux approximations [33]. Such conventional GKFS has inherent limitations. Specifically, their reliance on first-order expansions restricts their applicability to continuum flow regimes, because in the rarefied regime the constitutive relationships are highly nonlinear [34–37]. Thus, they cannot adequately capture nonequilibrium phenomena in rarefied gas dynamics.

B. Grad 13 function-based gas kinetic flux solver

To retain the nice feature of GKFS from the continuum regime to the rarefied regime, $f(\boldsymbol{x}_{I+1/2}-\boldsymbol{\xi}\Delta t,\boldsymbol{\xi},t)$ is constructed with the help of the Grad 13 distribution function, whose expression is given as

$$f^{G13}=g\left(1+\frac{\sigma_{ij}}{2pRT}C_iC_j+\frac{q_iC_i}{pRT}\left(\frac{C^2}{5RT}-1\right)\right), \tag{19}$$

in which the high-order moments σ_{ij} and q_i represent the stress and heat flux, respectively. Their moment relationships are given as

$$\sigma_{ij}=\langle C_{<i}C_{j>}f^{\mathrm{G13}}\rangle \quad\text{and}\quad q_i=\tfrac{1}{2}\langle C_iC^2f^{\mathrm{G13}}\rangle. \tag{20}$$

The angular bracket subscript shown in Eq. (20) means the trace-free part of a symmetric tensor as

$$C_{\langle i}C_{j\rangle} = C_iC_j - \tfrac{1}{3}\delta_{ij}C_kC_k. \tag{21}$$

From Eqs. (19) and (20), we can see that the Grad 13 distribution function is relevant to conservative variables $\mathbf{W}$ and high-order moments, including σ_{ij} and q_i. It is noted that conservative variables and high-order moments all belong to macroscopic variables. Hence, to construct the initial gas distribution function of f^{G13} at the surrounding points $\boldsymbol{x}_{I+1/2} - \boldsymbol{\xi}\Delta t$, we need to calculate these macroscopic variables at the points around the cell interface. Here, we adopt $A(\boldsymbol{x}_{I+1/2} - \boldsymbol{\xi}\Delta t, t)$ to represent those macroscopic variables around the vertical interface $\boldsymbol{x}_{I+1/2}$ at the beginning of each time step, and they can be calculated by

$$A(\boldsymbol{x}_{I+1/2} - \boldsymbol{\xi}\Delta t, t) = \begin{cases} A_L(\boldsymbol{x}_{I+1/2}, t) - \nabla A_L(\boldsymbol{x}_{I+1/2}, t)\cdot\boldsymbol{\xi}\Delta t, & \xi_x > 0 \\ A_R(\boldsymbol{x}_{I+1/2}, t) - \nabla A_R(\boldsymbol{x}_{I+1/2}, t)\cdot\boldsymbol{\xi}\Delta t, & \xi_x < 0 \end{cases}, \tag{22}$$

where the subscripts $\bullet_{\mathrm{L}}$ and $\bullet_{\mathrm{R}}$ are the values of macroscopic variables at the left and the right sides of the vertical interface, respectively. ∇A stands for the gradient of macroscopic variables, which can be calculated by the central difference scheme.

In the existing G13-GKFS [27], the high-order moments at the cell interface are calculated via the moment relationship directly. Taking the heat flux in the x-direction as an example, the G13-GKFS predicts it by

$$q_x = \frac{1}{2}\sum_\alpha w_\alpha C_{x,\alpha}\mathbf{C}_\alpha^2 f(\mathbf{x}_f, \boldsymbol{\xi}_\alpha, t). \tag{23}$$

By substituting the expression of gas distribution functions f^L, f^R, f^U, and f^B at four cell interfaces that enclose the control cell into Eq. (23), the heat flux at the left, right, upper, and bottom interfaces could be calculated as follows:

$$q_x^L = \frac{1}{2}\sum_\alpha w_\alpha C_{x,\alpha}\mathbf{C}_\alpha^2 f^L(\mathbf{x}_f, \boldsymbol{\xi}_\alpha, t), \tag{24}$$

$$q_x^R = \frac{1}{2}\sum_\alpha w_\alpha C_{x,\alpha}\mathbf{C}_\alpha^2 f^R(\mathbf{x}_f, \boldsymbol{\xi}_\alpha, t), \tag{25}$$

$$q_x^U = \frac{1}{2}\sum_\alpha w_\alpha C_{x,\alpha}\mathbf{C}_\alpha^2 f^U(\mathbf{x}_f, \boldsymbol{\xi}_\alpha, t), \tag{26}$$

$$q_x^B = \frac{1}{2}\sum_\alpha w_\alpha C_{x,\alpha}\mathbf{C}_\alpha^2 f^B(\mathbf{x}_f, \boldsymbol{\xi}_\alpha, t), \tag{27}$$

where the high-order Gauss–Hermite quadrature rule [38,39] is adopted for the integral. For a function $f(\xi)$, the integral approximation is shown below:

$$\int_{-\infty}^{+\infty} f(\xi)d\xi = \int_{-\infty}^{+\infty} e^{-\xi^2}\left[e^{\xi^2}f(\xi)\right]d\xi \approx \sum_{\alpha=1}^{Q} w_\alpha e^{\xi_\alpha^2} f(\xi_\alpha), \tag{28}$$

in which $e^{-\xi^2}$ denotes the weighting function. w_α represents the corresponding quadrature weight, and is evaluated by

$$w_\alpha = \frac{2^{Q-1}Q!\sqrt{\pi}}{Q^2[H_{Q-1}(\xi_\alpha)]^2}, \tag{29}$$

Here, $H_Q(\xi)$ is the Q^{th} Gauss-Hermite polynomial. $\xi_\alpha(\alpha{=}1, \ldots, Q)$ are the positive roots of $H_Q(\xi)$ and are used to discretize the particle velocity space. Then, the high-order moments, such

as q_x^C, at the cell center could be evaluated by averaging the values at the surrounding four cell interfaces as follows:

$$q_x^C = \frac{1}{4}\left(q_x^L + q_x^R + q_x^U + q_x^B\right). \tag{30}$$

This kind of methodology to update the high-order moments at the cell interface is simple and straightforward, but it may not be consistent with the evolution of 13-moment equations.

IV. MOMENT GAS KINETIC FLUX SOLVER

In 13-moment equations, the high-order moments are calculated by their evolution equations. Here, we can list the evolution equations for σ_{ij} and q_i as follows:

$$\frac{\partial \sigma_{ij}}{\partial t} + \{\ldots \text{spatial derivatives of moments} \ldots\} = -\frac{\sigma_{ij}}{\tau}, \tag{31}$$

$$\frac{\partial q_i}{\partial t} + \{\ldots \text{spatial derivatives of moments} \ldots\} = -\frac{2}{3}\frac{q_i}{\tau}. \tag{32}$$

It is noteworthy that the spatial derivatives of moments in Eqs. (31) and (32) are different. Their expressions can be derived by following the method shown in Appendix, which is very complicated [40]. As shown in Eqs. (31) and (32), the partial differential equations for σ_{ij} and q_i are complicated and difficult to numerically solve. Thus, we want to find a way to solve these equations from the microscopic perspective. Motivated by the gas kinetic flux solver, where the numerical flux for the conservative variables can be calculated by the moments of the distribution function at the cell interface, we can explore a way to calculate the numerical flux for σ_{ij} and q_i based on the moment relationships of the distribution function. In other words, we need to construct the evolution function for the high-order moments at the mesoscopic level.

A. Microscopic kinetic framework for the evolution of the higher-order moment system

By utilizing the explicit–implicit method (the convection term is treated by the explicit scheme, while the collision term is treated by the implicit scheme), Eq. (1) can be discretized as

$$\frac{f^{n+1} - f^n}{\Delta t} + \boldsymbol{\xi} \cdot \nabla f^n = \frac{g^{n+1} - f^{n+1}}{\tau}, \tag{33}$$

where the superscripts $\bullet^{\mathrm{n}}$ and $\bullet^{\mathrm{n+1}}$ represent the variables at the current time level and the predicted time level, respectively. g^{n+1} means the equilibrium distribution function at the predicted time step, which is based on the predicted value of macroscopic variables. Then, Eq. (33) can be reformulated into

$$f^{n+1} = \frac{\Delta t}{\Delta t + \tau} g^{n+1} + \frac{\tau}{\Delta t + \tau} f^n - \frac{\Delta t \cdot \tau}{\Delta t + \tau} \boldsymbol{\xi} \cdot \nabla f^n. \tag{34}$$

Following the idea of G13-GKFS, we further adopt the Grad 13 distribution function f^{G13} [as shown in Eq. (19)] to approximate f^n at the surrounding points of the cell interface. Thus, Eq. (34) can be rewritten as

$$f^{n+1} = \frac{\Delta t}{\Delta t + \tau} g^{n+1} + \frac{\tau}{\Delta t + \tau} f^{G13,n} - \frac{\Delta t \cdot \tau}{\Delta t + \tau} \boldsymbol{\xi} \cdot \nabla f^{G13,n}. \tag{35}$$

By multiplying Eq. (35) with vector $\boldsymbol{\varphi}^{\mathrm{stress}}$ and $\boldsymbol{\varphi}^{\mathrm{heat}}$, whose expressions can be expressed as

$$\boldsymbol{\varphi}^{\mathrm{stress}} = \begin{bmatrix} C_{\langle x} C_{x\rangle} & C_{\langle x} C_{y\rangle} & C_{\langle x} C_{z\rangle} \\ C_{\langle y} C_{x\rangle} & C_{\langle y} C_{y\rangle} & C_{\langle y} C_{z\rangle} \\ C_{\langle z} C_{x\rangle} & C_{\langle z} C_{y\rangle} & C_{\langle z} C_{z\rangle} \end{bmatrix} \quad \text{and} \quad \boldsymbol{\varphi}^{\mathrm{heat}} = \begin{bmatrix} C_x C^2/2 \\ C_y C^2/2 \\ C_z C^2/2 \end{bmatrix}, \tag{36}$$

and integrating the resultant equations over the whole velocity space, we have

$$\langle \boldsymbol{\varphi}^{\text{stress}} \cdot f^{n+1} \rangle = \frac{\Delta t}{\Delta t + \tau} \langle \boldsymbol{\varphi}^{\text{stress}} \cdot g^{n+1} \rangle + \frac{\tau}{\Delta t + \tau} \langle \boldsymbol{\varphi}^{\text{stress}} \cdot f^{G13,n} \rangle - \frac{\Delta t \cdot \tau}{\Delta t + \tau} \langle \boldsymbol{\varphi}^{\text{stress}} \cdot \boldsymbol{\xi} \cdot \nabla f^{G13,n} \rangle, \tag{37}$$

and

$$\langle \boldsymbol{\varphi}^{\text{heat}} \cdot f^{n+1} \rangle = \frac{\Delta t}{\Delta t + \tau} \langle \boldsymbol{\varphi}^{\text{heat}} \cdot g^{n+1} \rangle + \frac{\tau}{\Delta t + \tau} \langle \boldsymbol{\varphi}^{\text{heat}} \cdot f^{G13,n} \rangle - \frac{\Delta t \cdot \tau}{\Delta t + \tau} \langle \boldsymbol{\varphi}^{\text{heat}} \cdot \boldsymbol{\xi} \cdot \nabla f^{G13,n} \rangle. \tag{38}$$

From the gas kinetic theory, we know that the high-order moments, such as the stress tensor and heat flux, can be calculated by taking the relevant moments of the gas distribution function as

$$\boldsymbol{M}^{\text{stress}} = \begin{bmatrix} \sigma_{xx} & \sigma_{xy} & \sigma_{xz} \\ \sigma_{yx} & \sigma_{yy} & \sigma_{yz} \\ \sigma_{zx} & \sigma_{zy} & \sigma_{zz} \end{bmatrix} = \begin{bmatrix} \langle C_{\langle x} C_{x\rangle} f^{G13} \rangle & \langle C_{\langle x} C_{y\rangle} f^{G13} \rangle & \langle C_{\langle x} C_{z\rangle} f^{G13} \rangle \\ \langle C_{\langle y} C_{x\rangle} f^{G13} \rangle & \langle C_{\langle y} C_{y\rangle} f^{G13} \rangle & \langle C_{\langle y} C_{z\rangle} f^{G13} \rangle \\ \langle C_{\langle z} C_{x\rangle} f^{G13} \rangle & \langle C_{\langle z} C_{y\rangle} f^{G13} \rangle & \langle C_{\langle z} C_{z\rangle} f^{G13} \rangle \end{bmatrix}, \tag{39}$$

and

$$\boldsymbol{M}^{\text{heat}} = \begin{bmatrix} q_x \\ q_y \\ q_z \end{bmatrix} = \begin{bmatrix} \langle C_x C^2 f^{G13} \rangle / 2 \\ \langle C_y C^2 f^{G13} \rangle / 2 \\ \langle C_z C^2 f^{G13} \rangle / 2 \end{bmatrix}. \tag{40}$$

Considering that the high-order moments for equilibrium distribution function g vanish, we have $\langle \boldsymbol{\varphi}^{\text{stress}} \cdot g^{n+1} \rangle \equiv 0$ and $\langle \boldsymbol{\varphi}^{\text{heat}} \cdot g^{n+1} \rangle \equiv 0$. Hence, Eqs. (37) and (38) can be rewritten as

$$\boldsymbol{M}^{\text{stress},n+1} = \frac{\tau}{\Delta t + \tau} \boldsymbol{M}^{\text{stress},n} - \frac{\Delta t \cdot \tau}{\Delta t + \tau} \langle \boldsymbol{\varphi}^{\text{stress}} \cdot \boldsymbol{\xi} \cdot \nabla f^{G13,n} \rangle, \tag{41}$$

and

$$\boldsymbol{M}^{\text{heat},n+1} = \frac{\tau}{\Delta t + \tau} \boldsymbol{M}^{\text{heat},n} - \frac{\Delta t \cdot \tau}{\Delta t + \tau} \langle \boldsymbol{\varphi}^{\text{heat}} \cdot \boldsymbol{\xi} \cdot \nabla f^{G13,n} \rangle. \tag{42}$$

It is noteworthy that the matrix of stress tensors shown in Eq. (39) is inherently symmetric as follows:

$$\sigma_{xy} = \sigma_{yx}, \quad \sigma_{xz} = \sigma_{zx}, \quad \sigma_{yz} = \sigma_{zy}. \tag{43}$$

Additionally, the sum of normal stress components is zero as follows:

$$\sigma_{xx} + \sigma_{yy} + \sigma_{zz} = 0. \tag{44}$$

Thus, the stress tensor contains only five independent components. Consequently, the five independent governing equations for these components: σ_{xx}, σ_{yy}, σ_{xy}, σ_{xz}, and σ_{yz} can be written as follows:

$$\sigma_{xx}^{n+1} = \frac{\tau}{\Delta t + \tau} \sigma_{xx}^{n} - \frac{\Delta t \cdot \tau}{\Delta t + \tau} \langle C_{\langle x} C_{x\rangle} \cdot \boldsymbol{\xi} \cdot \nabla f^{G13,n} \rangle, \tag{45}$$

$$\sigma_{yy}^{n+1} = \frac{\tau}{\Delta t + \tau} \sigma_{yy}^{n} - \frac{\Delta t \cdot \tau}{\Delta t + \tau} \langle C_{\langle y} C_{y\rangle} \cdot \boldsymbol{\xi} \cdot \nabla f^{G13,n} \rangle, \tag{46}$$

$$\sigma_{xy}^{n+1} = \frac{\tau}{\Delta t + \tau} \sigma_{xy}^{n} - \frac{\Delta t \cdot \tau}{\Delta t + \tau} \langle C_{\langle x} C_{y\rangle} \cdot \boldsymbol{\xi} \cdot \nabla f^{G13,n} \rangle, \tag{47}$$

$$\sigma_{xz}^{n+1} = \frac{\tau}{\Delta t + \tau} \sigma_{xz}^{n} - \frac{\Delta t \cdot \tau}{\Delta t + \tau} \langle C_{\langle x} C_{z\rangle} \cdot \boldsymbol{\xi} \cdot \nabla f^{G13,n} \rangle, \tag{48}$$

$$\sigma_{yz}^{n+1} = \frac{\tau}{\Delta t + \tau} \sigma_{yz}^{n} - \frac{\Delta t \cdot \tau}{\Delta t + \tau} \langle C_{\langle y} C_{z\rangle} \cdot \boldsymbol{\xi} \cdot \nabla f^{G13,n} \rangle. \tag{49}$$

For the heat flux vector, all three components (q_x, q_y, and q_z) are independent. Equation (42) therefore provides the following three governing equations:

$$q_x^{n+1} = \frac{\tau}{\Delta t + \tau} q_x^n - \frac{\Delta t \cdot \tau}{\Delta t + \tau} \langle 1/2 \cdot C_x C^2 \cdot \boldsymbol{\xi} \cdot \nabla f^{G13,n} \rangle, \tag{50}$$

$$q_y^{n+1} = \frac{\tau}{\Delta t + \tau} q_y^n - \frac{\Delta t \cdot \tau}{\Delta t + \tau} \langle 1/2 \cdot C_y C^2 \cdot \boldsymbol{\xi} \cdot \nabla f^{G13,n} \rangle, \tag{51}$$

$$q_z^{n+1} = \frac{\tau}{\Delta t + \tau} q_z^n - \frac{\Delta t \cdot \tau}{\Delta t + \tau} \langle 1/2 \cdot C_z C^2 \cdot \boldsymbol{\xi} \cdot \nabla f^{G13,n} \rangle. \tag{52}$$

Considering the five differential equations for conservation of mass (ρ), momentum ($\rho \mathbf{u}$), and energy (ρE) as given in Eq. (11), the G13-MGKFS framework effectively solves a coupled system of 5 (stress) + 3 (heat flux) + 5 (conservation) = 13 equations.

B. Methodology to update higher-order moments

On the framework of FVM, Eqs. (41) and (42) can also be integrated over a control volume ΔV. Then, it can be reformulated as

$$\boldsymbol{M}^{\text{stress},n+1} = \frac{\tau}{\Delta t + \tau} \boldsymbol{M}^{\text{stress},n} - \frac{\Delta t \cdot \tau}{\Delta V \cdot (\Delta t + \tau)} \begin{bmatrix} \left(\boldsymbol{F}^{\text{stress}}_{x,I+1/2} - \boldsymbol{F}^{\text{stress}}_{x,I-1/2}\right) \cdot \Delta y \cdot \Delta z \\ + \left(\boldsymbol{F}^{\text{stress}}_{y,J+1/2} - \boldsymbol{F}^{\text{stress}}_{y,J-1/2}\right) \cdot \Delta x \cdot \Delta z \\ + \left(\boldsymbol{F}^{\text{stress}}_{z,K+1/2} - \boldsymbol{F}^{\text{stress}}_{z,K-1/2}\right) \cdot \Delta x \cdot \Delta y \end{bmatrix}, \tag{53}$$

and

$$\boldsymbol{M}^{\text{heat},n+1} = \frac{\tau}{\Delta t + \tau} \boldsymbol{M}^{\text{heat},n} - \frac{\Delta t \cdot \tau}{\Delta V \cdot (\Delta t + \tau)} \begin{bmatrix} \left(\boldsymbol{F}^{\text{heat}}_{x,I+1/2} - \boldsymbol{F}^{\text{heat}}_{x,I-1/2}\right) \cdot \Delta y \cdot \Delta z \\ + \left(\boldsymbol{F}^{\text{heat}}_{y,J+1/2} - \boldsymbol{F}^{\text{heat}}_{y,J-1/2}\right) \cdot \Delta x \cdot \Delta z \\ + \left(\boldsymbol{F}^{\text{heat}}_{z,K+1/2} - \boldsymbol{F}^{\text{heat}}_{z,K-1/2}\right) \cdot \Delta x \cdot \Delta y \end{bmatrix}, \tag{54}$$

in which $\boldsymbol{F}^{\text{stress}}_{x,I+1/2}$ and $\boldsymbol{F}^{\text{heat}}_{x,I+1/2}$ represent the flux matrix for the stress tensor and heat on the interface between cell I and cell $I+1$ in the x-direction. $\boldsymbol{F}^{\text{stress}}_{x,I-1/2}$ and $\boldsymbol{F}^{\text{heat}}_{x,I-1/2}$ represent the flux matrix for stress tensor and heat on the interface between cell $I-1$ and cell I, also in the x-direction. These fluxes are computed via moment integration of the gas distribution function $f_{I\pm1/2}$ at the corresponding interface. Thus, for the x-direction interface, the fluxes for the stress tensor and heat flux are expressed as

$$\boldsymbol{F}^{\text{stress}}_{x,I\pm1/2} = \langle \xi_x \cdot \boldsymbol{\varphi}^{\text{stress}} \cdot f_{I\pm1/2} \rangle, \tag{55}$$

and

$$\boldsymbol{F}^{\text{heat}}_{x,I\pm1/2} = \langle \xi_x \cdot \boldsymbol{\varphi}^{\text{heat}} \cdot f_{I\pm1/2} \rangle. \tag{56}$$

Here, we take $\boldsymbol{F}^{\text{stress}}_{x,I+1/2}$ as an example for illustration. By substituting Eq. (15) into Eq. (55), we have

$$\boldsymbol{F}^{\text{stress}}_{x,I+1/2} = \left\langle \xi_x \cdot \boldsymbol{\varphi}^{\text{stress}} \cdot \left(\frac{\Delta t}{\tau + \Delta t} g(x_{I+1/2}, \boldsymbol{\xi}, t + \Delta t) + \frac{\tau}{\tau + \Delta t} f^{G13}(x_{I+1/2} - \boldsymbol{\xi} \Delta t, \boldsymbol{\xi}, t) \right) \right\rangle. \tag{57}$$

By using the numerical quadrature, $\boldsymbol{F}^{\text{stress}}_{x,I+1/2}$ can be approximated by

$$\boldsymbol{F}^{\text{stress}}_{x,I+1/2} = \sum_{\alpha} w_\alpha \xi_{x,\alpha} \boldsymbol{\varphi}^{\text{stress}}_\alpha \cdot \left(\frac{\Delta t}{\tau + \Delta t} g(x_{I+1/2}, \boldsymbol{\xi}_\alpha, t + \Delta t) + \frac{\tau}{\tau + \Delta t} f^{G13}(x_{I+1/2} - \boldsymbol{\xi}_\alpha \Delta t, \boldsymbol{\xi}_\alpha, t) \right). \tag{58}$$

The flux calculation approach for the y-direction ($\boldsymbol{F}^{\text{stress}}_{y,J+1/2}$, $\boldsymbol{F}^{\text{stress}}_{y,J-1/2}$, $\boldsymbol{F}^{\text{heat}}_{y,J+1/2}$, and $\boldsymbol{F}^{\text{heat}}_{y,J-1/2}$) and the z-direction ($\boldsymbol{F}^{\text{stress}}_{z,K+1/2}$, $\boldsymbol{F}^{\text{stress}}_{z,K-1/2}$, $\boldsymbol{F}^{\text{heat}}_{z,K+1/2}$, and $\boldsymbol{F}^{\text{heat}}_{z,K-1/2}$) follows identical principles to the x-direction implementation and is therefore omitted for brevity. Equations (53) and (54) are equivalent to Eqs. (31) and (32).

C. Implementation of boundary conditions

The Maxwellian boundary condition [41,42] is a rather simple model, based on which Gu [43] and Struchtrup [44] successfully constructed the macroscopic boundary conditions for regularized 13-moment equations, respectively. The macroscopic boundary conditions for the moment equations are very complicated. However, from the mesoscopic level, we just need to obtain the distribution function at the wall and then calculate the numerical fluxes on the boundary. Here, we also adopt the Maxwellian boundary condition. The coordinates are attached to the wall with the normal vector ($\mathbf{n}_i$) of the wall pointing toward the gas. All molecules with ($\xi_i \mathbf{n}_i < 0$) are incident upon the wall with a Grad 13 distribution function f^{G13} and molecules with ($\xi_i \mathbf{n}_i \geqslant 0$) are emitted by the wall with a Maxwellian distribution function f^w_M at the wall temperature (T_w) and wall velocity ($\mathbf{U}_w$). Hence, the distribution function reflected from the wall can be given with the equilibrium state as [45]

$$f^w_M = \frac{\rho_w}{2\pi R T_w} e^{-\frac{(\xi_i - \mathbf{U}_w)^2}{2RT_w}}. \tag{59}$$

Here, ρ_w represents the density at the wall and will be calculated later.

Based on the no-penetration condition, the relationship between incident and reflected gas distribution functions at the wall can be formulated as follows:

$$\int_{\xi_i n_i < 0} \xi_i f^{G13} d\xi_i + \int_{\xi_i n_i \geqslant 0} \xi_i f^w_M d\xi_i = 0. \tag{60}$$

By substituting Eq. (59) into Eq. (60), we have

$$\rho_w = -2\pi R T_w \frac{\int_{\xi_i n_i < 0} \xi_i f^{G13} d\xi_i}{\int_{\xi_i n_i \geqslant 0} \xi_i e^{-\frac{(\xi_i - \mathbf{U}_w)^2}{2RT_w}} d\xi_i}. \tag{61}$$

With ρ_w calculated, the reflecting distribution function f^w_M shown in Eq. (59) can be determined. Then, the gas distribution function and numerical fluxes at the wall can be evaluated.

D. Computational procedure

The computational sequence of the present moment gas kinetic flux solver can be summarized as follows:

(1) Discretize the physical space and particle velocity space by $\mathbf{x}_i$ and ξ_α, respectively.

(2) Calculate the initial macroscopic variables around the cell interface with Eq. (22). Then, reconstruct the initial Grad 13 distribution function at the surrounding points $f(\boldsymbol{x}_{I+1/2} - \boldsymbol{\xi}\Delta t, \boldsymbol{\xi}, t)$ of each cell interface with Eq. (19).

(3) Compute the conservative variables $\vec{W}_{I+1/2}$ at the cell interface using Eq. (16). Then, construct the distribution function $g(\boldsymbol{x}_{I+1/2}, \xi, t)$ at the equilibrium state with Eq. (2).

(4) With $f(\boldsymbol{x}_{I+1/2} - \boldsymbol{\xi}\Delta t, \boldsymbol{\xi}, t)$ and $g(\boldsymbol{x}_{I+1/2}, \xi, t)$ known, we can reconstruct the distribution function $f(\boldsymbol{x}_{I+1/2}, \boldsymbol{\xi}, t + \Delta t)$ at the cell interface using Eq. (15).

(5) Implement appropriate boundary conditions by constructing the incident and reflected gas distribution function at the wall, as shown in Sec. IV C.

(6) Calculate the numerical flux for conservative variables with Eq. (9), and calculate the numerical flux for high-order moments with Eq. (57).

(7) Update the conservative flow variables with Eq. (13) and update the high-order moments following the equations shown in Eqs. (53) and (54).

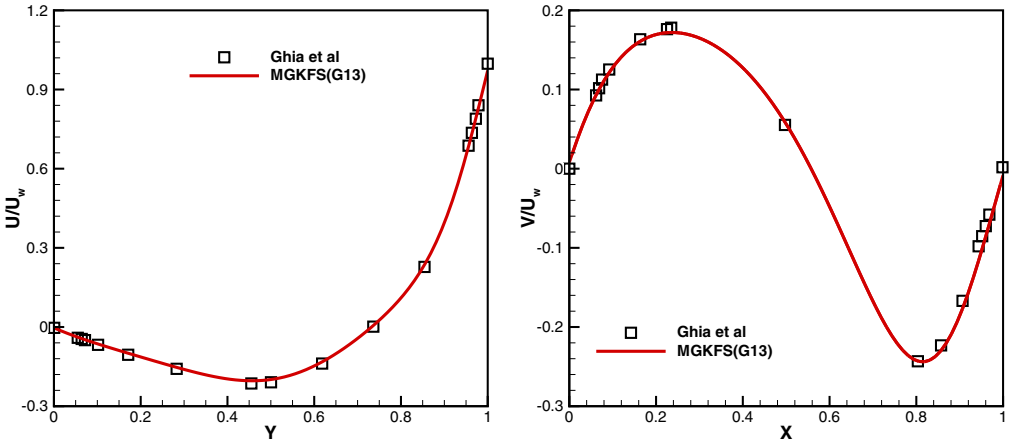

FIG. 2. Comparison of velocity profiles along centerlines for Re = 100. (a) U-velocity profiles along vertical centerline and (b) V-velocity profiles along horizontal centerline.

(8) Repeat steps (2)–(7) until the computation converges or the prescribed maximum computational time is reached.

V. NUMERICAL VALIDATIONS

In this section, a series of numerical simulations for flows from the continuum regime to the transition regimes is conducted to validate the computational accuracy and efficiency of the proposed MGKFS. The DVM results are taken as the primary benchmark data. Furthermore, the results obtained from G13-GKFS are also adopted as the reference data to validate the performance of the present MGKFS.

Case 1: Lid-driven cavity flow. The first test example is a two-dimensional lid-driven cavity flow, whose schematic illustration depicts a square enclosure with a length L, as detailed in Ref. [46]. In this setup, the top wall is in motion with a velocity of $U_w = 50\,\mathrm{m/s}$, while the remaining walls keep stationary. All walls are presumed to be isothermal and maintain a constant temperature of $T_w = 273\,\mathrm{K}$. This case effectively reflects the rarefaction effect, and was thus simulated by Liu *et al*. [28] using the G13-GKFS. Here, the computational domain is uniformly segmented into 60×60 cells, and the particle velocity space is discretized using 8×8 quadrature points.

To validate the performance of the current solver in the continuum regime, we consider test cases with Reynolds numbers of Re = 100, 400, and 1000. As the Reynolds number increases, the computational domain is uniformly divided into 80×80, 100×100, and 120×120 cells, respectively. The reference viscosity μ_0 is derived from the Reynolds number using the formula $\mu_0 = \rho_0 U_w L/Re$. As shown in Fig. 2, the velocity profiles predicted by the present solver align closely with those reported by Ghia *et al*. [47] at Re = 100. When the Reynolds number is increased to 400, as illustrated in Fig. 3, the velocity profiles predicted by the present solver can still match well with the results given by Ghia *et al*. As illustrated in Fig. 4, comparison of velocity profiles along centerlines indicates that the present solver can still recover the results from Ghia *et al*. [47] for Re = 1000. These test cases validate that the present solver yields accurate results in the continuum regime.

The comparison of temperature contours and heat flux lines at Kn = 0.0798 (belonging to the rarefied regime) is illustrated in Fig. 5. Notably, the present solver demonstrates excellent capability in predicting the anti-Fourier heat transfer phenomenon, where heat flux propagates from cold to warm regions, achieving comparable accuracy with both the DVM and the G13-GKFS results.

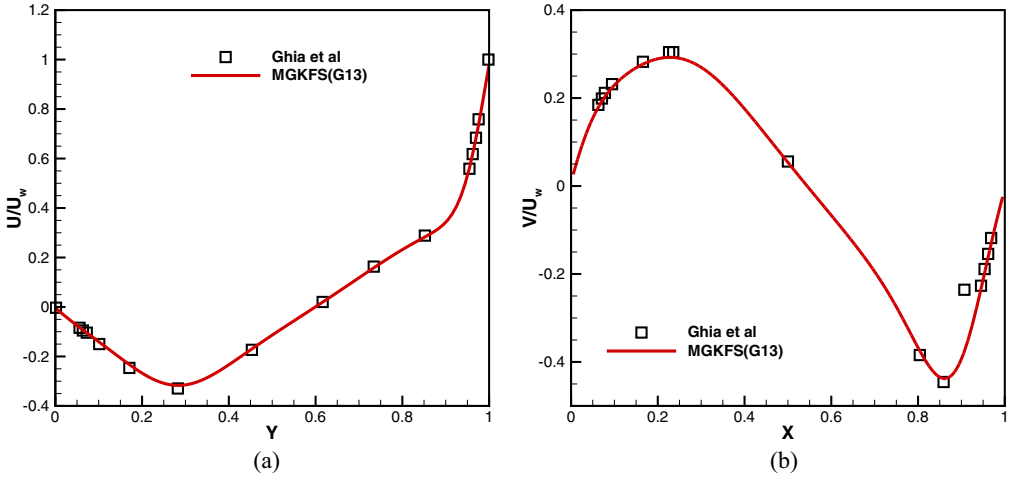

FIG. 3. Comparison of velocity profiles along centerlines for Re = 400. (a) U-velocity profiles along vertical centerline and (b) V-velocity profiles along horizontal centerline.

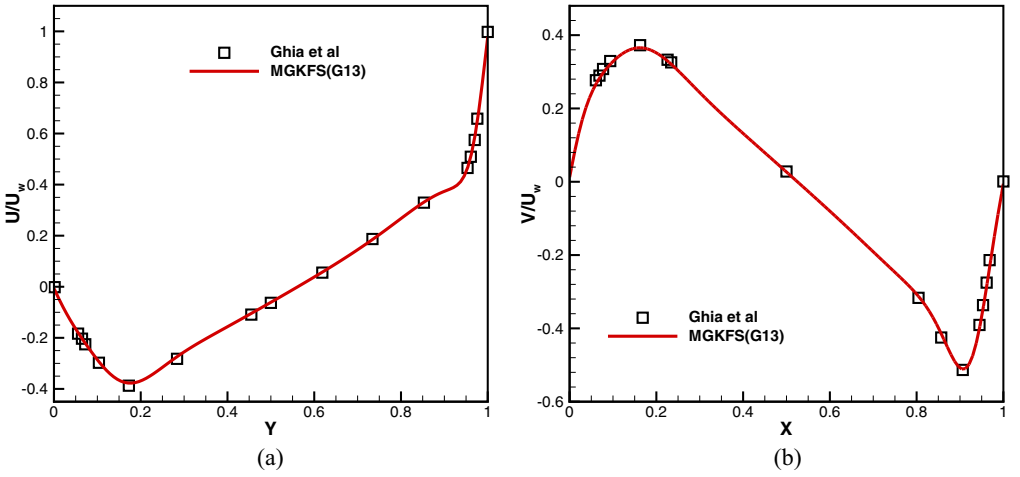

FIG. 4. Comparison of velocity profiles along centerlines for Re = 1000. (a) U-velocity profiles along vertical centerline and (b) V-velocity profiles along horizontal centerline.

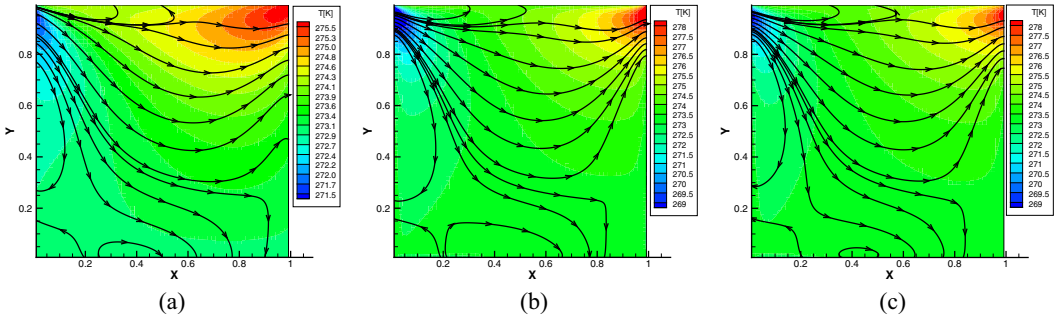

FIG. 5. Comparison of temperature contours and heat flux lines. (a) DVM, (b) G13-GKFS and (c) MGKFS.

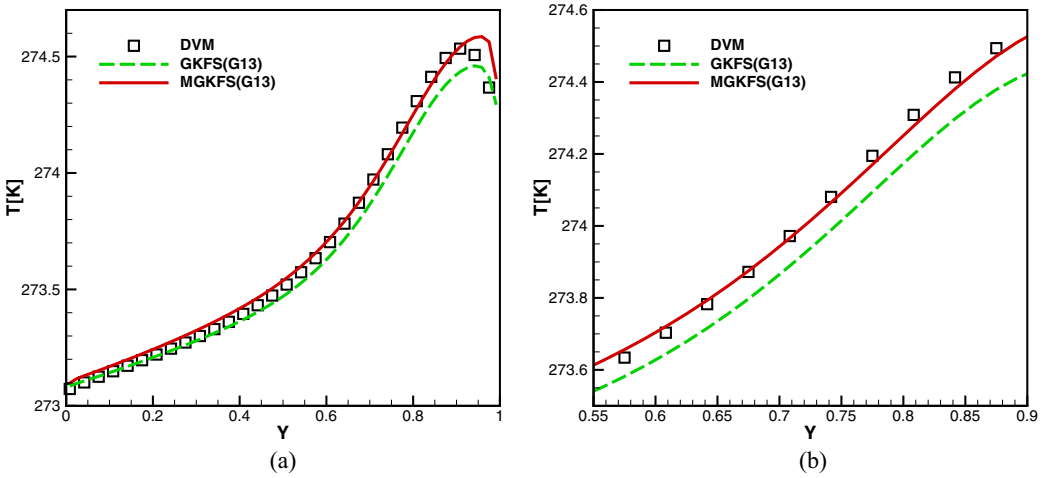

FIG. 6. Comparison of temperature profiles by different schemes at Kn = 0.0798. (a) Temperature profiles along vertical central and (b) Locally zoom profiles along vertical lines central lines.

Figure 6 provides quantitative comparisons of temperature profiles along vertical central lines for different schemes. When benchmarked against the reference data, the present MGKFS demonstrates superior performance to the G13-GKFS.

To further validate the proposed method, the comparative contours of the stress tensor component σ_{xy} is shown in Fig. 7. The visual comparison reveals agreement among results from different computational schemes. Subsequent analysis focuses on the profile of the stress tensor within the top boundary layer. As shown in Fig. 8, the stress tensor (σ_{xx} and σ_{xy}) predicted by MGKFS is in better agreement with DVM data than results given by G13-GKFS.

Subsequently, we conduct a comparative analysis of heat flux profiles along both the x-direction (q_x) and the y-direction (q_y) components through vertical central lines, as illustrated in Fig. 9. The zoom views presented in Figs. 9(a) and 9(b) reveal that the MGKFS demonstrates superior alignment with the DVM compared to G13-GKFS. This comparative study validates the enhanced accuracy of the proposed solver over conventional G13-GKFS in predicting key thermal parameters. The improved performance can be attributed to the present treatment of high-order moments through microscopic evolution functions, which enable more precise modeling of complex thermal transport phenomena.

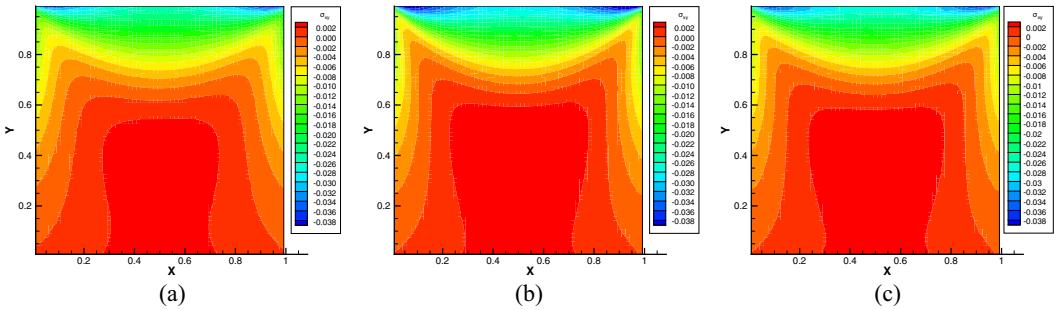

FIG. 7. Comparison of stress tensor contour (σ_{xy}) by different schemes at Kn = 0.0798. (a) DVM, (b) G13-GKFS, and (c) MGKFS.

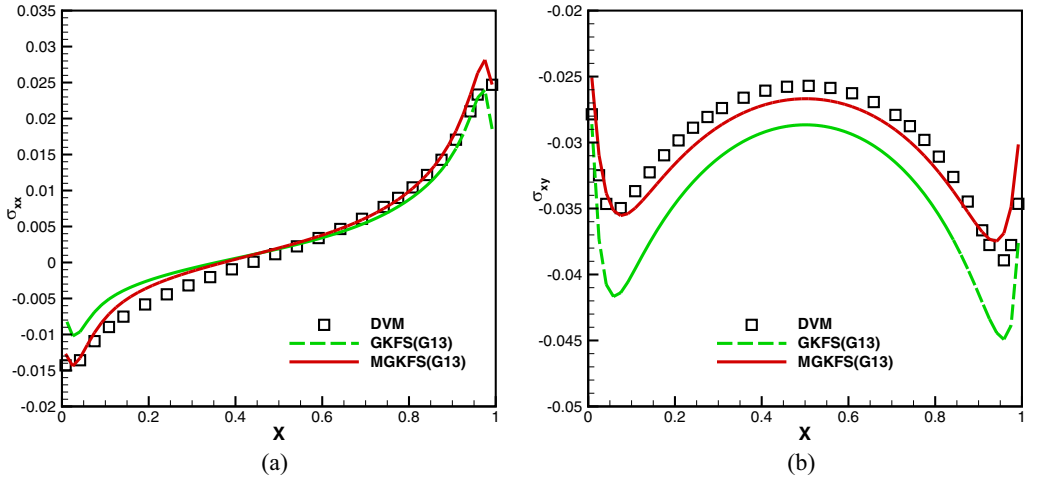

FIG. 8. Comparison of profiles for stress tensor by different schemes at Kn = 0.0798. (a) Profiles for stress tensor (σ_{xx}) within bottom boundary and (b) Profiles for stress tensor (σ_{xy}) within bottom boundary.

The convergence rate for this case is presented in Fig. 10. The figure demonstrates that the G13-GKFS and MGKFS achieve the same convergence rate, which is superior to that of the DVM solver. As listed in Table I, the MGKFS matches the G13-GKFS in efficiency and surpasses the DVM solver.

Case 2: Bottom-heated cavity flow. The lid-driven cavity flows typically exhibit minimal thermal variation. In the second test example, we consider a more rigorous validation case involving thermally driven flows induced by a bottom-heated wall. The benchmark configuration consists of a square cavity with side length L. A thermal boundary condition is imposed such that the bottom wall maintains an elevated temperature of $T_0 + \Delta T$ (where $T_0 = 300\,\mathrm{K}$ denotes reference temperature and $\Delta T = 300\,\mathrm{K}$ represents the temperature difference), while all other walls remain fixed at T_0. To systematically evaluate the performance of MGKFS in rarefied flow regimes, simulations

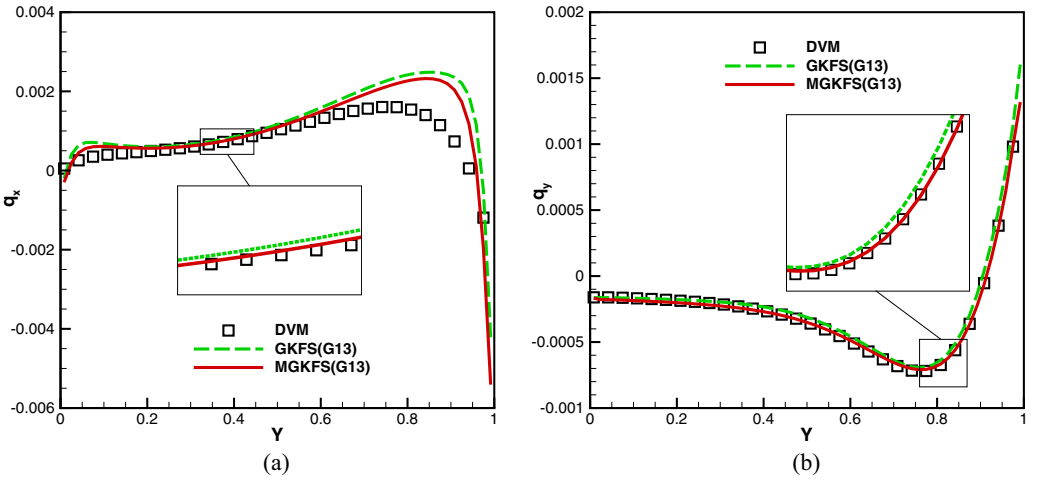

FIG. 9. Comparison of heat flux along vertical centerline. (a) Profiles for heat flux in x-direction along vertical central lines and (b) Profiles for heat flux in y-direction along vertical central lines.

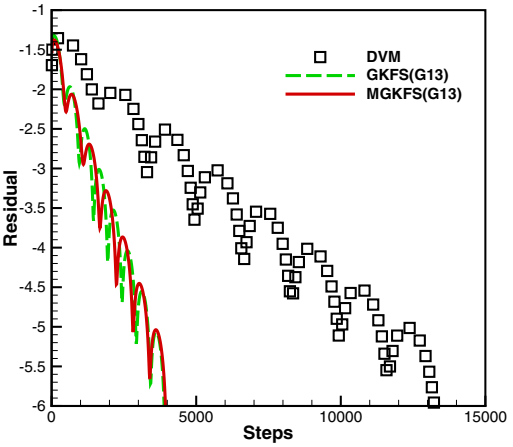

FIG. 10. Comparison of convergence rates by different schemes for lid-driven cavity flow.

are conducted at Knudsen numbers of 0.13. The computational domain is divided uniformly into 60×60 cells. The numerical integration accuracy is enhanced by employing 28×28 points in the velocity space. For preserving comparability with reference solutions, the viscosity coefficient μ is calculated following the formulation described in Ref. [28]. As displayed in Fig. 11, the flow patterns predicted by DVM, G13-GKFS, and MGKFS agree well with each other. The temperature profiles along both horizontal and vertical central lines, as illustrated in Fig. 12, are also matched very well.

Subsequent comparisons of the heat flux reveal significant performance differences between different schemes. As evidenced in Fig. 13(a), it is obvious that the MGKFS demonstrates superior accuracy in predicting heat flux along the horizontal central line, compared to G13-GKFS. The result along the vertical central line [Fig. 13(b)] reinforces this trend, with MGKFS outperforming all G13-GKFS in heat flux prediction accuracy. Figure 13(c) demonstrates that MGKFS heat flux profiles in the x-direction (q_x) within the boundary layer are in better agreement with DVM results than the G13-GKFS. The heat flux in the y-direction (q_y) as shown in Fig. 13(d) further validates this trend: MGKFS demonstrates improved accuracy in predicting the y-directional heat flux profile when compared against the DVM data, showing significant improvements over the G13-GKFS results.

Case 3: Temperature gradient-driven flow. The final validation case evaluates solver performance for thermally driven flows induced by temperature gradients, previously investigated by Yang *et al.* [48] using moment methods. The computational domain consists of a square cavity with initial density $\rho = 1.0$. The left and right walls maintain a constant temperature $T_{\text{low}} = 263\,\text{K}$, while the top and bottom walls exhibit a piecewise linear temperature distribution: temperature increases linearly from T_{low} to $T_{high} = 283\,\text{K}$ along the first half of each wall, then decreases linearly back to T_{low} over the second half. The dynamic viscosity follows Sutherland's law [49]. The Knudsen

TABLE I. Comparison of computational time (seconds) by different schemes for the lid-driven cavity flow at Kn = 0.0798.

Schemes	Time	Steps	Time per step
DVM	8382.7	13 240	0.633
G13-GKFS	252.3	3890	0.065
MGKFS	283.5	3940	0.072

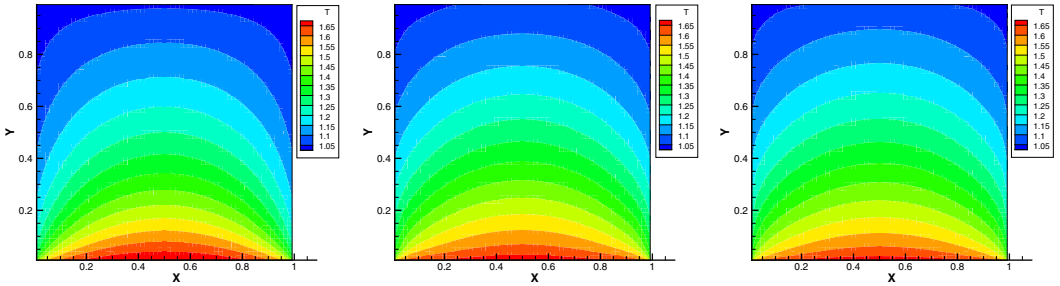

(a) (b) (c)

FIG. 11. Comparison of temperature contours by different schemes at Kn = 0.13. (a) DVM, (b) G13-GKFS, and (c) MGKFS.

number (Kn = 0.1) is examined in this rarefied flow regime. To ensure accuracy of numerical integration, we increased quadrature points in the velocity space to 16 × 16 (previous tests with 8 × 8 showed insufficient precision). Figure 14 compares temperature field predictions from the MGKFS, G13-GKFS, and DVM. All methods demonstrate excellent agreement in temperature profiles. Figure 14 presents the temperature profiles along the horizontal and vertical centerlines predicted by different methods in panels (a) and (b), respectively. Both panels demonstrate that MGKFS, G13-GKFS, and DVM agree well with each other.

The comparison of contours for heat flux by different methods is shown in Fig. 15, which shows the similar spatial distributions in heat flux. The comparison of heat flux (q_x) along horizontal central lines and heat flux (q_y) along vertical centerlines is shown in Figs. 16(a) and 16(b), respectively. The present MGKFS achieves better correlation with DVM benchmark data than G13-GKFS. Additionally, quantitative boundary-layer analyses reveal significant improvements. As shown in Figs. 16(c) and 16(d), within the bottom boundary, the present MGKFS results exhibit fine correlation with DVM data, significantly outperforming the G13-GKFS. As illustrated in Figs. 16(e) and 16(f), the heat flux (q_x and q_y) predicted by MGKFS exhibits closer agreement with the DVM results compared to those from G13-GKFS. The progressive accuracy enhancement from G13-GKFS to

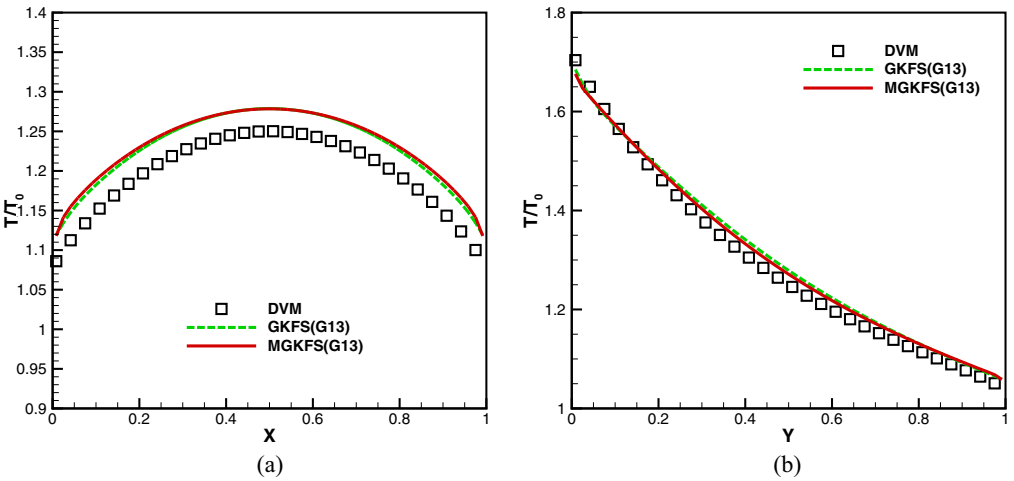

(a) (b)

FIG. 12. Comparison of temperature profiles by different schemes at Kn = 0.13. (a) Temperature profiles along horizontal central lines and (b)Temperature profiles along vertical central lines.

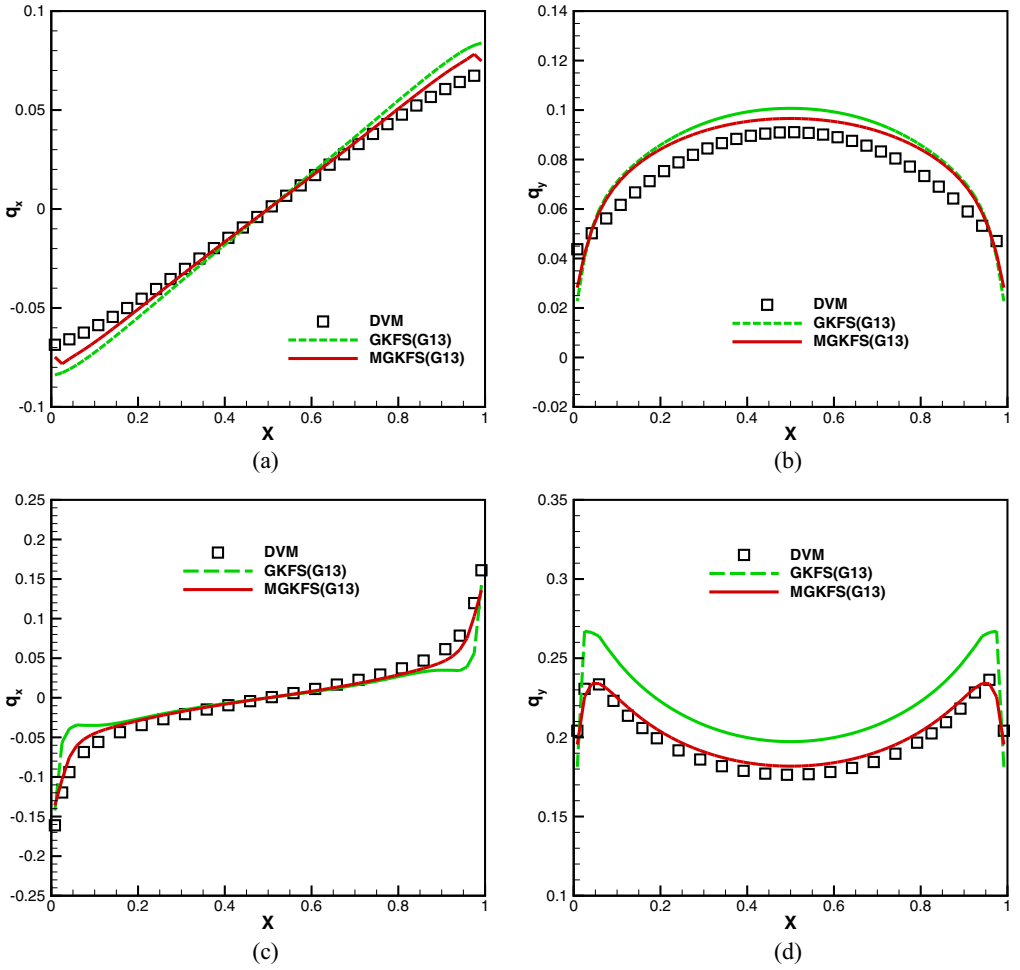

FIG. 13. Comparison of profiles for heat flux by different schemes at Kn = 0.13. (a) Profiles for heat flux (q_x) along horizontal central lines, (b) Profiles for heat flux (q_y) along horizontal central lines, (c) Profiles for heat flux (q_x) within bottom boundary, and (d) Profiles for heat flux (q_y) within bottom boundary.

MGKFS suggests that the evolution for high-order moments can improve the accuracy of heat flux calculations.

The convergence rates of DVM, G13-GKFS, and MGKFS are compared in Fig. 17. It is evident that the convergence rate of the present solver is roughly the same as that of the G13-GKFS and

TABLE II. Comparison of computational time (seconds) by different schemes for temperature gradient-driven flow at Kn = 0.1.

Schemes	Time	Steps	Time Per Step
DVM	54 229.6	13 010	4.168
G13-GKFS	1250.1	4540	0.275
MGKFS	1305.8	4610	0.283

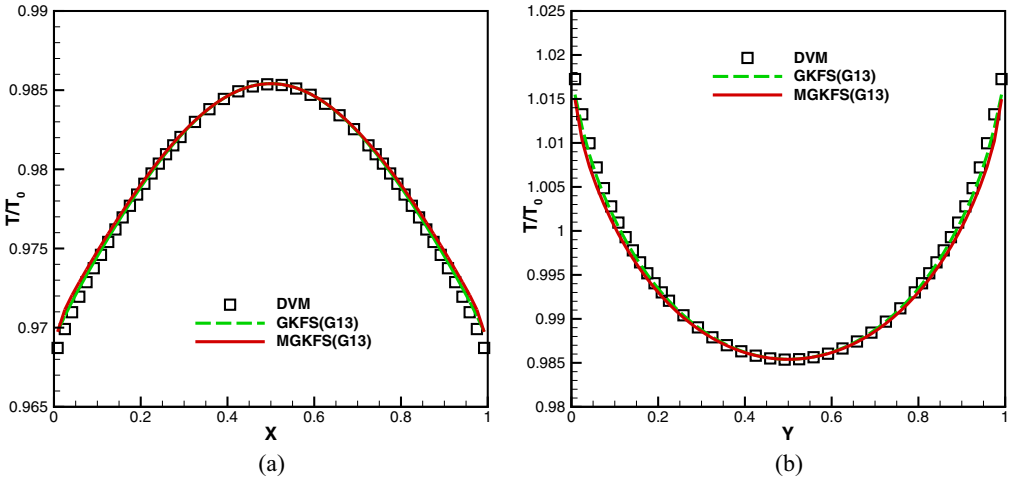

FIG. 14. Comparison of temperature profiles by different schemes at Kn = 0.1. (a) Temperature profiles along horizontal central lines and (b) Temperature profiles along vertical central lines.

is faster than the DVM. Comparisons of computational time are presented in Table II. The results demonstrate that the MGKFS are much more efficient than the DVM.

VI. CONCLUDING REMARKS

This paper presents the MGKFS for simulating flows from continuum regimes to rarefied regimes. MGKFS solves evolution equations governing mass, momentum, energy, stress, and heat flux. By solving this comprehensive set of equations, it ensures global solution fidelity for all flow quantities, thereby overcoming a limitation inherent to the G13-GKFS—namely, insufficient global or localized accuracy for stress and heat flux. Furthermore, MGKFS circumvents the need to directly solve the high-order PDEs in the 13-moment system and eliminates the complex boundary conditions. Numerical results demonstrate the enhanced accuracy of MGKFS in capturing high-order moments compared to G13-GKFS, particularly in critical regions such as boundary layers. Furthermore, MGKFS exhibits a convergence rate and computational cost comparable to G13-GKFS while maintaining its efficiency benefits, and superior to the DVM. These attributes establish MGKFS as a highly promising tool for efficient multi-scale flow simulations.

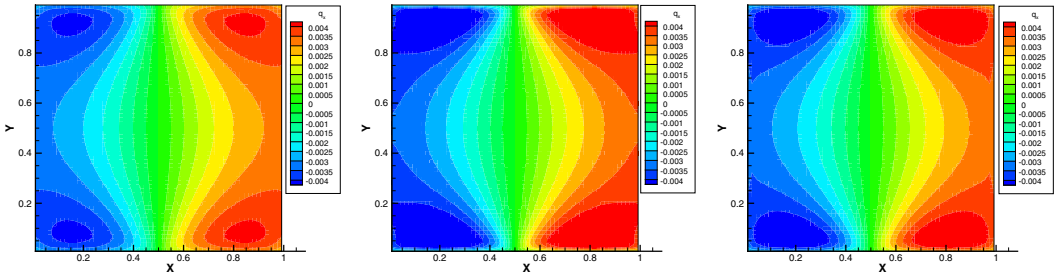

FIG. 15. Comparison of contours for heat flux in x-direction (q_x) at Kn = 0.1. (a) DVM, and (b) G13-GKFS, (c) MGKFS.

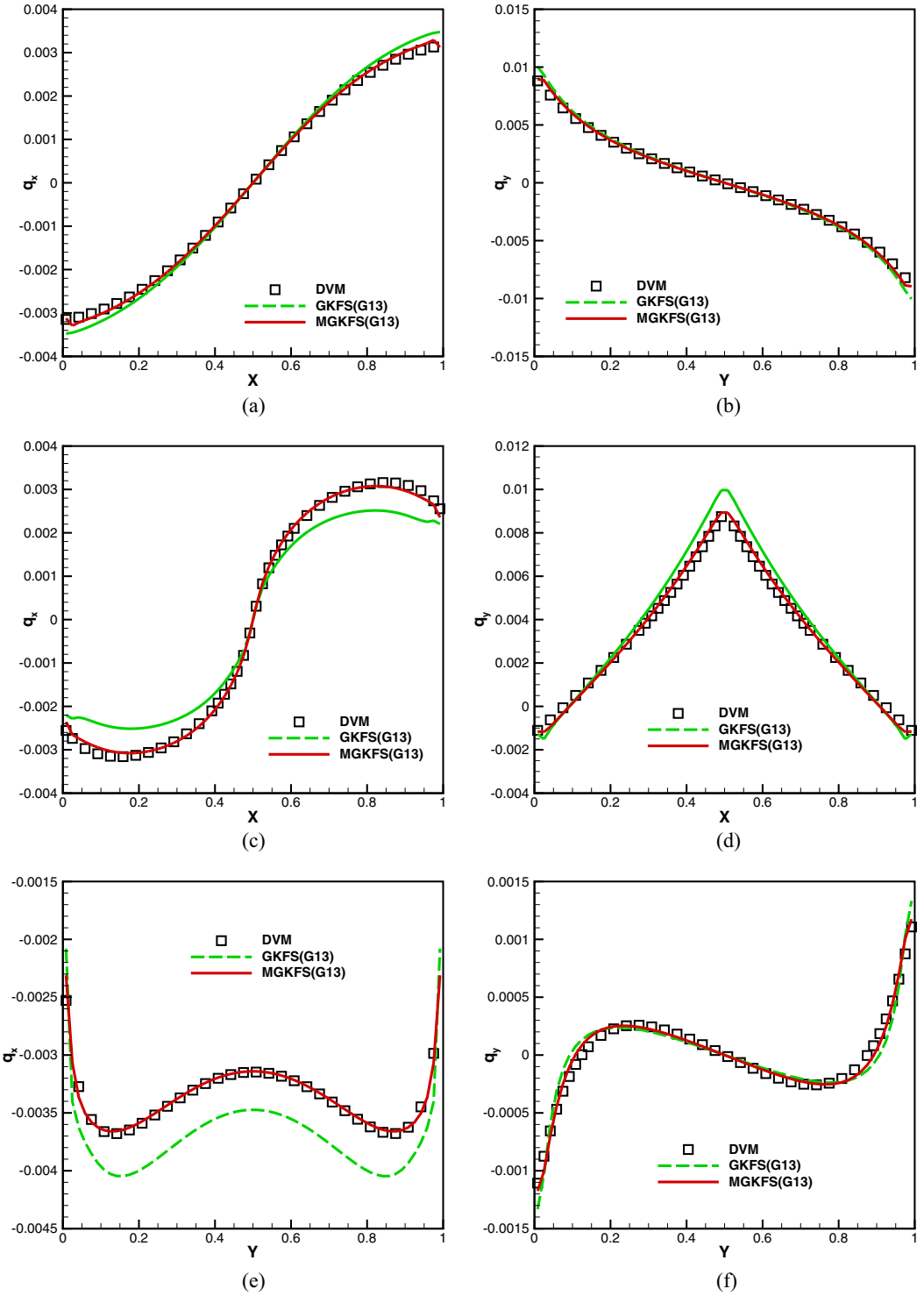

FIG. 16. Comparison of profiles for heat flux by different schemes at Kn = 0.1. (a) Profiles for heat flux (q_x) along horizontal central lines and (b) Profiles for heat flux (q_y) along vertical central lines, (c) Profiles for heat flux (q_x) within bottom boundary, and (d) Profiles for heat flux (q_y) within bottom boundary, (e) Profiles for heat flux (q_x) within left boundary, and (f) Profiles for heat flux (q_y) within left boundary.

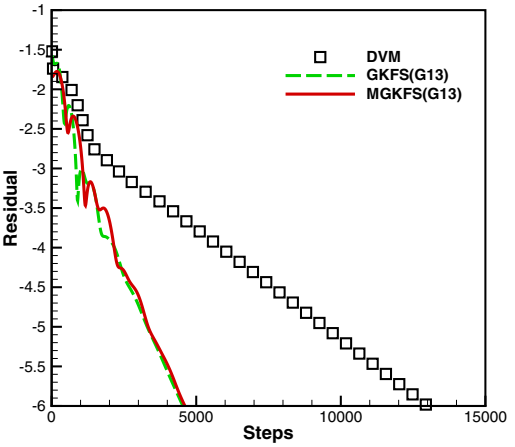

FIG. 17. Comparison of convergence rates by different schemes for temperature gradient-driven flow.

ACKNOWLEDGMENTS

This research is supported by the National Natural Science Foundation of China (Grants No. 12302376 and No. 92571301), the Natural Science Foundation of Jiangsu Province (Grant No. BK20230905), and the Shanghai Key Lab of Vehicle Aerodynamics and Vehicle Thermal Management Systems (Grant No. VATLAB-2025-3).

DATA AVAILABILITY

The data that support the findings of this article are not publicly available. The data are available from the authors upon reasonable request.

APPENDIX: DERIVATION OF MACROSCOPIC GOVERNING EQUATIONS FROM MOMENTS OF DISTRIBUTION FUNCTIONS

According to the moment relationships shown in Eq. (5), we have

$$F_x^{\rho} = \langle \xi_x \cdot f \rangle = \rho U. \tag{A1}$$

By substituting $\xi_x = U + C_x$ into $\langle \xi_x \cdot f \rangle$, we have

$$\langle \xi_x \cdot f \rangle = \langle (U + C_x) \cdot f \rangle = U \cdot \langle f \rangle + \langle C_x \cdot f \rangle = \rho U + \langle C_x \cdot f \rangle. \tag{A2}$$

By comparing Eq. (A1) and Eq. (A2), we know that

$$\langle C_x \cdot f \rangle \equiv 0. \tag{A3}$$

Similarly, we can have

$$\langle C_y \cdot f \rangle \equiv 0 \quad \text{and} \quad \langle C_z \cdot f \rangle \equiv 0. \tag{A4}$$

Furthermore, by substituting $\xi_x = U + C_x$ into $\langle \xi_x \cdot \xi_x \cdot f \rangle$, we have

$$F_x^{\rho U} = \langle \xi_x \cdot \xi_x \cdot f \rangle = \langle (U + C_x)^2 \cdot f \rangle = \rho U^2 + 2U \cdot \langle C_x \cdot f \rangle + \langle C_x{}^2 \cdot f \rangle. \tag{A5}$$

By substituting Eq. (A3) into Eq. (A5), we have

$$F_x^{\rho U} = \langle \xi_x \cdot \xi_x \cdot f \rangle = \langle (U + C_x)^2 \cdot f \rangle = \rho U^2 + \langle C_x{}^2 \cdot f \rangle. \tag{A6}$$

Then, the moment $\langle {C_x}^2 \cdot f \rangle$ can be split, written as

$$\left\langle {C_x}^2 \cdot f \right\rangle = \left\langle \left({C_x}^2 + {C_y}^2 + {C_z}^2 \right)/3 \cdot f \right\rangle + \left\langle \left(2 \cdot {C_x}^2 - {C_y}^2 - {C_z}^2 \right)/3 \cdot f \right\rangle. \tag{A7}$$

By substituting the moment relationships of pressure (p) and stress tensor component (σ_{xx})

$$p = \left\langle \left({C_x}^2 + {C_y}^2 + {C_z}^2 \right)/3 \cdot f \right\rangle \quad \text{and} \quad \sigma_{xx} = \left\langle \left(2 \cdot {C_x}^2 - {C_y}^2 - {C_z}^2 \right)/3 \cdot f \right\rangle, \tag{A8}$$

into Eq. (A7), the moment $\langle {C_x}^2 \cdot f \rangle$ can be rewritten as

$$\left\langle {C_x}^2 \cdot f \right\rangle = p + \sigma_{xx}. \tag{A9}$$

Finally, by substituting Eq. (A9) into Eq. (A6), we can obtain the macroscopic expression for $F_x^{\rho U}$ as follows:

$$F_x^{\rho U} = \rho U^2 + p + \sigma_{xx}. \tag{A10}$$

In the same way, we can derive the microscopic expressions for $F_x^{\rho V}$ and $F_x^{\rho W}$, as follows:

$$F_x^{\rho V} = \langle \xi_x \cdot \xi_y \cdot f \rangle = \rho UV + \langle C_x C_y f \rangle = \rho UV + \sigma_{xy}, \tag{A11}$$

$$F_x^{\rho W} = \langle \xi_x \cdot \xi_z \cdot f \rangle = \rho UW + \langle C_x C_z f \rangle = \rho UW + \sigma_{xz}. \tag{A12}$$

The toughest work is to derive the macroscopic expression for $F_x^{\rho E}$, which can be expanded into three parts:

$$F_x^{\rho E} = \tfrac{1}{2}\left(\left\langle \xi_x \cdot \xi_x^2 \cdot f \right\rangle + \left\langle \xi_x \cdot \xi_y^2 \cdot f \right\rangle + \left\langle \xi_x \cdot \xi_z^2 \cdot f \right\rangle \right). \tag{A13}$$

Then, by substituting $\xi_x = U + C_x$ into $\langle \xi_x \cdot \xi_x^2 \cdot f \rangle$, we have

$$\begin{aligned} \left\langle \xi_x \cdot \xi_x^2 \cdot f \right\rangle &= \langle (U + C_x)^3 \cdot f \rangle = \left\langle \left(U^3 + C_x^3 + 3 \cdot U \cdot C_x^2 + 3 \cdot C_x \cdot U^2 \right) \cdot f \right\rangle \\ &= U^3 \cdot \langle f \rangle + \left\langle C_x^3 \cdot f \right\rangle + 3U \cdot \left\langle C_x^2 \cdot f \right\rangle + 3 \cdot U^2 \langle C_x \cdot f \rangle. \end{aligned} \tag{A14}$$

Considering $\langle f \rangle = \rho$ and $\langle C_x \cdot f \rangle \equiv 0$, Eq. (A14) can be reformulated as

$$\left\langle \xi_x^3 \cdot f \right\rangle = \rho \cdot U^3 + \left\langle C_x^3 \cdot f \right\rangle + 3U \cdot \left\langle C_x^2 \cdot f \right\rangle. \tag{A15}$$

Similarly, by substituting $\xi_x = U + C_x$ and $\xi_y = V + C_y$ into $\langle \xi_x \cdot \xi_y^2 \cdot f \rangle$, we have

$$\begin{aligned} \left\langle \xi_x \cdot \xi_y^2 \cdot f \right\rangle &= \langle (U + C_x)(V + C_y)^2 \cdot f \rangle \\ &= U \cdot V^2 \cdot \langle f \rangle + U \cdot \left\langle C_y^2 \cdot f \right\rangle + 2U \cdot V \cdot \langle C_y \cdot f \rangle \\ &\quad + V^2 \cdot \langle C_x \cdot f \rangle + \left\langle C_y^2 \cdot C_x \cdot f \right\rangle + 2V \cdot \langle C_x \cdot C_y \cdot f \rangle. \end{aligned} \tag{A16}$$

Considering $\langle f \rangle = \rho$, $\langle C_x \cdot f \rangle \equiv 0$, $\langle C_y \cdot f \rangle \equiv 0$, and $\langle C_x \cdot C_y \cdot f \rangle = \sigma_{xy}$, Eq. (A16) can be reformulated as

$$\left\langle \xi_x \cdot \xi_y^2 \cdot f \right\rangle = \rho \cdot U \cdot V^2 + U \cdot \left\langle C_y^2 \cdot f \right\rangle + \left\langle C_x \cdot C_y^2 \cdot f \right\rangle + 2V \cdot \sigma_{xy}. \tag{A17}$$

Similarly, $\langle \xi_x \cdot \xi_z^2 \cdot f \rangle$ can be written as

$$\left\langle \xi_x \cdot \xi_z^2 \cdot f \right\rangle = \rho \cdot U \cdot W^2 + U \cdot \left\langle C_z^2 \cdot f \right\rangle + \left\langle C_x \cdot C_z^2 \cdot f \right\rangle + 2W \cdot \sigma_{xz}. \tag{A18}$$

By substituting Eqs. (A15), (A17), and (A18) into Eq. (A13), we have

$$F_x^{\rho E} = \frac{1}{2} \begin{pmatrix} \rho \cdot U \cdot (U^2 + V^2 + W^2) + \left\langle C_x \cdot \left(C_x^2 + C_y^2 + C_z^2 \right) \cdot f \right\rangle \\ +2U \cdot \left\langle C_x^2 \cdot f \right\rangle + U \cdot \left\langle \left(C_x^2 + C_y^2 + C_z^2 \right) \cdot f \right\rangle + 2V \cdot \sigma_{xy} + 2W \cdot \sigma_{xz} \end{pmatrix}. \tag{A19}$$

Considering $\langle C_x \cdot (C_x^2 + C_y^2 + C_z^2) f \rangle = 2q_x$, $\langle C_x^2 \cdot f \rangle = p + \sigma_{xx}$[as indicated in Eq. (A9)], and $\langle (C_x^2 + C_y^2 + C_z^2) \cdot f \rangle = 3p$, $F_x^{\rho E}$ can be reformulated as

$$\begin{aligned} F_x^{\rho E} &= \frac{1}{2}\begin{pmatrix} \rho \cdot U \cdot (U^2 + V^2 + W^2) + 2q_x + 2U \cdot p \\ +3U \cdot p + 2U \cdot \sigma_{xx} + 2V \cdot \sigma_{xy} + 2W \cdot \sigma_{xz} \end{pmatrix} \\ &= U \cdot \left(\frac{1}{2}\rho \cdot (U^2 + V^2 + W^2) + \frac{3}{2}p \right) + q_x + U \cdot p + U \cdot \sigma_{xx} + V \cdot \sigma_{xy} + W \cdot \sigma_{xz}. \end{aligned} \tag{A20}$$

As shown in Eq. (6), $E = (U^2 + V^2 + W^2)/2 + RT/(\gamma - 1)$. By using the relations that $\gamma = 5/3$ and $p = \rho RT$, we have

$$E = (U^2 + V^2 + W^2)/2 + 3p/(2\rho). \tag{A21}$$

Thus, Eq. (A20) can be finally expressed as

$$F_x^{\rho E} = U \cdot (\rho E + p) + \sigma_{xx} \cdot U + \sigma_{xy} \cdot V + \sigma_{xz} \cdot W + q_x. \tag{A22}$$

By combining Eqs. (A1), (A10), (A11), (A12), and (A22) in the matrix $\vec{F}_x$, we can obtain the relations shown in Eq. (10). The macroscopic expression for $\vec{F}_y$ and $\vec{F}_z$ can be derived in the same way shown above. Here, we list the final results as follows:

$$\vec{F}_y = \begin{bmatrix} \rho V \\ \rho V U + \sigma_{yx} \\ \rho V^2 + p + \sigma_{yy} \\ \rho V W + \sigma_{yz} \\ V(\rho E + p) + \sigma_{yx} U + \sigma_{yy} V + \sigma_{yz} W + q_y \end{bmatrix}, \tag{A23}$$

and

$$\vec{F}_z = \begin{bmatrix} \rho W \\ \rho W U + \sigma_{zx} \\ \rho W V + \sigma_{zy} \\ \rho W^2 + p + \sigma_{zz} \\ W(\rho E + p) + \sigma_{zx} U + \sigma_{zy} V + \sigma_{zz} W + q_z \end{bmatrix}. \tag{A24}$$

[1] Z. Yuan, W. Zhao, Z. Jiang, W. Chen, and R. K. Agarwal, Modified nonlinear coupled constitutive relations model for hypersonic nonequilibrium flows, J. Thermophys. Heat Tr. **34**, 848 (2020).

[2] Z. Jiang, W. Zhao, Z. Yuan, W. Chen, and R. Myong, Computation of hypersonic flows over flying configurations using a nonlinear constitutive model, AIAA J. **57**, 5252 (2019).

[3] Y. Zhang, S. Dou, J. Qi, X. Xu, J. Qiu, and Z. Wei, Experimental study on slip flow of nitrogen through microchannels at atmospheric pressure, Microfluid. Nanofluid. **27**, 7 (2023).

[4] M. Akbari and M. Ghasemi, A novel kinetic-based slip velocity boundary condition suitable for compressible gas flows in micro-/nanochannels, Acta Mech. **229**, 4471 (2018).

[5] S. Varoutis, D. Valougeorgis, O. Sazhin, and F. Sharipov, Rarefied gas flow through short tubes into vacuum, J. Vac. Sci. Technol. A **26**, 228 (2008).

[6] O. Sazhin, Rarefied gas flow into vacuum through a channel with sudden contraction or expansion, Microfluid. Nanofluid. **24**, 76 (2020).

[7] G. A. Bird, *Molecular Gas Dynamics and the Direct Simulation of Gas Flows* (Clarendon Press, Oxford, 1994).

[8] Z. Yuan, W. Zhao, and W. Chen, Numerical study of heat flux reduction mechanism of the counterflowing jet in rarefied flows, in *AIP Conference Proceedings* (AIP Publishing, Glasgow, UK, 2019), p. 030003.

[9] M. H. Gorji and P. Jenny, A Fokker–Planck based kinetic model for diatomic rarefied gas flows, Phys. Fluids **25**, 062002 (2013).
[10] F. Fei, Z. Liu, J. Zhang, and C. Zheng, A particle Fokker-Planck algorithm with multiscale temporal discretization for rarefied and continuum gas flows, Commun. Comput. Phys. **22**, 338 (2017).
[11] C. Liu, Y. Zhu, and K. Xu, Unified gas-kinetic wave-particle methods I: Continuum and rarefied gas flow, J. Comput. Phys. **401**, 108977 (2020).
[12] Y. Zhu, C. Liu, C. Zhong, and K. Xu, Unified gas-kinetic wave-particle methods. II. Multiscale simulation on unstructured mesh, Phys. Fluids **31**, 067105 (2019).
[13] S. Liu, C. Zhong, and M. Fang, Simplified unified wave-particle method with quantified model-competition mechanism for numerical calculation of multiscale flows, Phys. Rev. E **102**, 013304 (2020).
[14] L. Yang, C. Shu, J. Wu, and Y. Wang, Numerical simulation of flows from free molecular regime to continuum regime by a DVM with streaming and collision processes, J. Comput. Phys. **306**, 291 (2016).
[15] L. Yang, C. Shu, W. Yang, Z. Chen, and H. Dong, An improved discrete velocity method (DVM) for efficient simulation of flows in all flow regimes, Phys. Fluids **30**, 062005 (2018).
[16] X. Gu and D. Emerson, A high-order moment approach for capturing non-equilibrium phenomena in the transition regime, J. Fluid Mech. **636**, 177 (2009).
[17] A. Rana, M. Torrilhon, and H. Struchtrup, A robust numerical method for the R13 equations of rarefied gas dynamics: Application to lid driven cavity, J. Comput. Phys. **236**, 169 (2013).
[18] A. Rana, A. Mohammadzadeh, and H. Struchtrup, A numerical study of the heat transfer through a rarefied gas confined in a microcavity, Continuum Mech. Therm. **27**, 433 (2015).
[19] K. Xu and J. Huang, A unified gas-kinetic scheme for continuum and rarefied flows, J. Comput. Phys. **229**, 7747 (2010).
[20] S. Liu, P. Yu, K. Xu, and C. Zhong, Unified gas-kinetic scheme for diatomic molecular simulations in all flow regimes, J. Comput. Phys. **259**, 96 (2014).
[21] W. Su, L. Zhu, and L. Wu, Fast convergence and asymptotic preserving of the general synthetic iterative scheme, SIAM J. Sci. Comput. **42**, B1517 (2020).
[22] J. Zeng, R. Yuan, Y. Zhang, Q. Li, and L. Wu, General synthetic iterative scheme for polyatomic rarefied gas flows, Computers & Fluids **265**, 105998 (2023).
[23] Z. Guo, R. Wang, and K. Xu, Discrete unified gas kinetic scheme for all Knudsen number flows. II. Thermal compressible case, Phys. Rev. E **91**, 033313 (2015).
[24] Z. Xin, Y. Zhang, C. Zhang, and Z. Guo, Multiscale discrete Maxwell boundary condition for the discrete unified gas kinetic scheme for all Knudsen number flows, Phys. Rev. E **112**, 045316 (2025).
[25] Z. Liu, L. Yang, C. Shu, S. Chen, M. Wan, W. Liu, and Z. Yuan, Explicit formulations of G13-based gas kinetic flux solver (G13-GKFS) for simulation of continuum and rarefied flows, Phys. Fluids **33**, 037133 (2021).
[26] Z. Liu, C. Shu, S. Chen, W. Liu, Z. Yuan, and L. Yang, Development of explicit formulations of G45-based gas kinetic scheme for simulation of continuum and rarefied flows, Phys. Rev. E **105**, 045302 (2022).
[27] Z. Yuan, C. Shu, and Z. Liu, Grad's distribution functions-based gas kinetic scheme for simulation of flows beyond Navier–Stokes level, Phys. Fluids **33**, 122007 (2021).
[28] Z. Liu, C. Shu, S. Chen, L. Yang, M. Wan, and W. Liu, A novel solver for simulation of flows from continuum regime to rarefied regime at moderate Knudsen number, J. Comput. Phys. **415**, 109548 (2020).
[29] Z. Yuan, L. Yang, C. Shu, K. Jiang, and Z. Chen, Complete third-order polynomial expansion-based gas kinetic flux solver for flows from continuum regime to rarefied regime, Phys. Fluids **35**, 122011 (2023).
[30] Z. Yuan, Z. Chen, C. Shu, Y. Liu, and Z. Zhang, A novel construction of distribution function through second-order polynomial approximation in terms of particle mass, momentum and energy, Adv. Appl. Math. Mech. **16**, 738 (2024).
[31] Y. Liu, L. Yang, C. Shu, Z. Zhang, and Z. Yuan, An implicit high-order radial basis function-based differential quadrature-finite volume method on unstructured grids to simulate incompressible flows with heat transfer, J. Comput. Phys. **467**, 111461 (2022).
[32] Z. Yuan, L. Yang, C. Shu, Z. Liu, and W. Liu, A novel gas kinetic flux solver for simulation of continuum and slip flows, Int. J. Numer. Meth. Fl **93**, 2863 (2021).

[33] Z. Yuan, W. Zhao, Z. Jiang, and W. Chen, Numerical simulation of hypersonic reaction flows with nonlinear coupled constitutive relations, Aerosp. Sci. Technol. **112**, 106591 (2021).
[34] S. Zeng, Z. Yuan, W. Zhao, and W. Chen, Numerical simulation of hypersonic thermochemical nonequilibrium flows using nonlinear coupled constitutive relations, Chin. J. Aeronaut. **36**, 63 (2023).
[35] S. Zeng, J. Yang, W. Zhao, Z. Yuan, G. Fan, and W. Chen, Nonlinear coupled constitutive relations for hypersonic reacting flows with thermal nonequilibrium effect, Phys. Fluids **37**, 016116 (2025).
[36] Z. Yuan, K. Jiang, S. Zeng, Z. Jiang, and W. Chen, Topology of Nonlinear Coupled Constitutive Relations and Comparison of Different Iterative Methods, in *International Conference on Computational & Experimental Engineering and Sciences* (Springer, 2024), pp. 389–406.
[37] Z. Yuan, Z. Jiang, W. Zhao, and W. Chen, Analysis of gas flow over a cylinder at all Knudsen numbers based on non-Newtonian constitutive models, Int. J. Mod. Phys. B **34**, 2040076 (2020).
[38] G. Golub and J. Welsch, Calculation of Gauss quadrature rules, Math. Comput. **23**, 221 (1969).
[39] B. Shizgal, A Gaussian quadrature procedure for use in the solution of the Boltzmann equation and related problems, J. Comput. Phys. **41**, 309 (1981).
[40] H. Struchtrup and M. Torrilhon, Regularization of Grad's 13 moment equations: Derivation and linear analysis, Phys. Fluids **15**, 2668 (2003).
[41] C. Cercignani and M. Lampis, Kinetic models for gas-surface interactions, Transport Theor. Stat. **1**, 101 (1971).
[42] Z. Li, W. Hu, A. Peng, J. Wu, and C. Lee, Gas-kinetic unified algorithm for plane external force-driven flows covering all flow regimes by modeling of Boltzmann equation, Int. J. Numer. Meth. Fl **92**, 922 (2020).
[43] X. Gu and D. Emerson, A computational strategy for the regularized 13 moment equations with enhanced wall-boundary conditions, J. Comput. Phys. **225**, 263 (2007).
[44] M. Torrilhon and H. Struchtrup, Boundary conditions for regularized 13-moment-equations for micro-channel-flows, J. Comput. Phys. **227**, 1982 (2008).
[45] W. Liu, Y. Liu, L. Yang, Z. Liu, Z. Yuan, C. Shu, and C. Teo, Coupling improved discrete velocity method and G13-based gas kinetic flux solver: A hybrid method and its application for non-equilibrium flows, Phys. Fluids **33**, 092007 (2021).
[46] Z. Yuan, L. Yang, C. Shu, K. Jiang, and L. Zhang, A variant of improved discrete velocity method for efficient simulation of flows in entire Knudsen number regimes, Phys. Fluids **36**, 022018 (2024).
[47] U. Ghia, K. N. Ghia, and C. T. Shin, High-Re solutions for incompressible flow using the Navier-Stokes equations and a multigrid method, J. Comput. Phys. **48**, 387 (1982).
[48] W. Yang, X. Gu, D. R. Emerson, Y. Zhang, and S. Tang, Modelling thermally induced non-equilibrium gas flows by coupling kinetic and extended thermodynamic methods, Entropy **21**, 816 (2019).
[49] Z. Yuan, Z. Jiang, W. Zhao, and W. Chen, Multiple temperature model of nonlinear coupled constitutive relations for hypersonic diatomic gas flows, AIP Advances **10**, 055023 (2020).